Circuits, Systems, and Signal Processing (2024) 43:408–456
https://doi.org/10.1007/s00034-023-02479-z

An Optimized Dual Image Watermarking Scheme based on Redundant DWT and Randomized SVD with Henon Mapping Encryption

Ranjana Dwivedi[1] · Divyanshu Awasthi[1] · Vinay Kumar Srivastava[1]

Received: 23 March 2023 / Revised: 27 July 2023 / Accepted: 27 July 2023 /
Published online: 14 August 2023

Abstract
Imperceptibility, embedding capacity and robustness are basic requirements of an image watermarking algorithm. There is always a trade-off among these requirements. To achieve a balance between these three properties in an image watermarking scheme, this paper presents a high capacity and encrypted dual image watermarking in YCbCr color space. This scheme is based on redundant discrete wavelet transform (RDWT), randomized singular value decomposition (RSVD), Manta ray foraging optimization (MRFO) and Henon mapping. Further, MRFO is utilized to get the optimized strength factor for embedding the watermark into the cover image to achieve high robustness and imperceptibility along with desired capacity. The luminance component of cover image is used to embed the watermark as it contains the vital information. Performance of the proposed scheme is evaluated for various medical and non-medical images in terms of imperceptibility and robustness. Different quality metrics are utilized to assess the performance of scheme. Various attacks are applied to check the robustness of the proposed method. Imperceptibility and robustness along with embedding capacity and computational complexity comparison with existing techniques are also presented. The comparison of MRFO with particle swarm optimization (PSO) is also carried out. Peak signal-to-noise ratio (PSNR) for all cover images is above 60 dB whereas Structural similarity index measure (SSIM) and Normalized correlation (NC) values are above 0.99 under no attacks. For non-medical images, the average percentage improvement in PSNR is 13.76% and in NC is 4.3% in comparison with other existing schemes.

✉ Ranjana Dwivedi
ranjana@mnnit.ac.in

Divyanshu Awasthi
divyanshu.2021rel04@mnnit.ac.in

Vinay Kumar Srivastava
vinay@mnnit.ac.in

[1] Department of Electronics and Communication Engineering, Motilal Nehru National Institute of Technology Allahabad, Prayagraj, India

In case of medical images, average percentage improvement in PSNR is 41.35% and in NC is 0.62% when compared with related works. The proposed scheme is less computational complex in comparison with other existing schemes.

Keywords RDWT · RSVD · MRFO · YCbCr

1 Introduction

As communication networks quickly expand, digital image transmission over the Internet is increasing day by day. It is becoming progressively prevalent in our digital world, with the rise of social media, streaming services and other online platforms that allow users to share and utilize digital images. Telemedicine is a fast-evolving field of clinical care where medical data is transmitted via interactive media for consultations and occasionally for remote medical treatments or tests. In order to send medical images from one location to another and provide medical expertise, tele-radiology is an important area of telemedicine. Digital communication technology is initially unreliable for secure online image communication due to disturbances generated across the communication channel and different hacker actions. Due to the value of the medical images and the high cost of data collection, security of the medical image has become essential. Although there are several data hiding systems developed for tele-radiology applications, image watermarking techniques are employed to protect patient confidentiality. Digital image watermarking has become increasingly important due to the ease of copying and distributing digital images over the Internet. It is used in various applications to provide copyright protection, image authentication, tamper detection, and content identification.

Digital image watermarking [1–16] is the process of embedding a digital watermark, which is a unique identifier or code, into an image to protect its authenticity, ownership, or copyright. The watermark can be visible or invisible, and it is difficult to remove or alter without damaging the image quality. While designing an image watermarking algorithm, parameters such as capacity, security, imperceptibility and robustness must be considered. Several image watermarking techniques have been proposed in the literature. Recent techniques in digital image watermarking are based on deep learning, transform and compressive sensing techniques. Deep learning-based watermarking [2, 6] uses deep learning models to embed a watermark into an image. The models can be trained to embed the watermark in a way that makes it more robust to various image processing attacks. In multi-layer watermarking, multiple watermarks are embedded into an image at different layers. Each layer has a different level of complexity, making it more difficult for attackers to remove or alter the watermarks. Compressive sensing-based watermarking [12] uses compressive sensing theory to embed a watermark into an image. The technique is more efficient than traditional watermarking methods and provides better resistance to various attacks.

Transform domain watermarking involves embedding the watermark into cover image in the transform domain using the discrete cosine transform (DCT) [17], discrete wavelet transform (DWT) [1], RDWT [4, 18], lifting wavelet transform (LWT) [19] and integer wavelet transform (IWT) [20]. The transform domain provides a more robust and efficient way to embed the watermark. Researchers also proposed watermarking techniques based on the combination of these transforms to achieve better imperceptibility and robustness. To provide robust watermarking technique, these transforms are also combined with singular value decomposition (SVD) such as DWT-SVD [21], DWT-DCT-SVD [22], RDWT-SVD [4], LWT-SVD [14, 19] and IWT-SVD [20]. Security of watermarking algorithms can be enhanced by applying encryption of watermark during embedding. Various encryption techniques are utilized in image watermarking to enhance the security [18, 23]. Many techniques have been suggested in the literature for authentication and copyright protection of gray scale images, while for color images, limited schemes have been proposed in the literature.

Table 1 tabulates the recent proposed techniques and its objective, limitations based on hybrid transforms. A review of the literature indicates that an appropriate combination of transform domain techniques can increase the robustness of the image watermarking scheme, and a scrambled watermark can offer additional security. Therefore, this paper introduces a dual image watermarking based on RDWT-RSVD-MRFO using Henon mapping encryption in YCbCr color space. Luminance component of cover image is utilized to embed both watermarks. Strength factor is optimized using MRFO. During embedding, both watermarks are encrypted using Henon mapping to enhance the security of proposed method. To assess the imperceptibility and robustness of proposed method, quality metrics such as PSNR, SSIM, Kullback–Leibler divergence (KL DIV), Jensen–Shannon divergence (JS DIV), NC and bit error rate (BER) are calculated.

There are several benefits of the below-mentioned state of the literature survey but many issues yet needed to be resolved. Following are the problems listed below:

(1) Lack of security is the major concern in most of the existing schemes. To provide the copyright protection, watermarks need to be secured with proper encryption techniques.
(2) Capacity is another concern of dual image watermarking technique. High capacity is the need of efficient watermarking scheme.
(3) Balance among the resilience, imperceptibility and capacity is the vital requirement of watermarking. So, to achieve a balance between these parameters an optimized scaling factor is needed.
(4) Computational complexity and cost are high in many of the previously existing techniques.
(5) In several techniques, shift-variant and slow DWT is used to transform the images.
(6) False-positive problem is another major concern of many techniques.

Following are the major contributions of the proposed work:

(1) YCbCr color space is preferred over conventional RGB as Y (luminance) component contains the collective brightness of all three channels, i.e., R, G and B. Any forgery or alteration in Y component can be visible through naked eye. YCbCr color space also has very less effect of noise.
(2) RDWT is used in place of traditional DWT as RDWT is having the property of shift invariance. It is also used to enhance the capacity of the proposed method.

Table 1 Literature survey of some recent state-of-the-art image watermarking schemes

References	Objective	Scheme	Attacks	Findings	Limitation
[24]	For the purpose of hiding multiple watermarks, an improved DWT-SVD with hamming code watermarking technique that is non-blind, robust, imperceptible and secure is presented	SVD, DWT and Hamming code	Salt and pepper noise, Gaussian noise, Rotation, JPEG compression, speckle noise, cropping, median filter, histogram equalization	By embedding multiple watermarks in a medical cover image utilizing the DWT-SVD domain, the paper presents an improved watermarking technique that can secure patient data	Proposed technique does not perform well when subjected to a cropping attack in the case of chaotic LZW
[25]	Developed a reliable, effective and secure dual watermarking technique for medical CT scan images	RDWT and randomized singular value decomposition (RSVD)	Speckle noise, salt and pepper noise, Gaussian noise, median filter, histogram equalization, sharpening, JPEG compression, cropping, rotation, scaling, translation	Hybrid nature-inspired techniques are utilized to find the optimal scaling factor. It utilizes DWT to incorporate the system's media access control address in the image of the patient's ID card to produce the final mark	BER is much high under cropping, histogram equalization, scaling sharpening attacks
[19]	Robust and imperceptible hybrid domain image watermarking schemes is proposed	LWT, DWT, DCT, SVD	Noise attacks, filtering attacks, JPEG compression, region of interest filtering, geometric attacks, image processing operations	LWT-DCT-SVD- and DWT-DCT-SVD-based image watermarking scheme is presented. JAYA and PSO optimization techniques are utilized to find the suitable scaling factor	Embedding capacity of proposed scheme is not discussed

Table 1 (continued)

References	Objective	Scheme	Attacks	Findings	Limitation
[22]	A hybrid blind robust digital image watermarking technique integrating DCT, three-level DWT, and SVD was presented to ensure multimedia security	DCT, DWT and SVD	Wiener, average, median filter, salt and pepper noise, rotation, row/column delete attack	Performance analysis of presented scheme is evaluated against various filters and attacks by varying window size and noise density. Security is provided by applying Arnold Transform on watermark before embedding	High computational complexity in terms of time and space
[26]	To include a watermark into an image, discrete stationary wavelet transform and singular value decomposition are utilized	Stationary wavelet transform (SWT) and SVD	Gaussian filter, median filter, wiener filter, salt and pepper noise, speckle noise	SWT divides one image into numerous levels. Approximation, horizontal, vertical and diagonal levels are generated for each level	Watermark embedding and extraction computation times are not taken into account
[27]	Proposed an imperceptible, robust and blind image watermarking scheme for red-cyan anaglyph images	DWT, fast Walsh–Hadamard transform (FWHT) and SVD	Gaussian noise, Average filter, Sharpening, JPEG compression, Color quantization, Scaling, Gamma correction, histogram equalization, resizing	The technique attempts to extract an effective feature to incorporate the watermark using DWT, Hadamard transform and SVD	There is no discussion of the suggested scheme's computational complexity

Table 1 (continued)

References	Objective	Scheme	Attacks	Findings	Limitation
[28]	To propose an evolutionary programming method for applying a watermarking system to secure medical images	Improved discrete wavelet transform (IDWT), SVD and particle swarm optimization (PSO)	Salt and Pepper attack, Speckle noise, Gaussian attack, Rescaling, Histogram Equalization, Gamma Correction, Rotation, Gaussian Low-Pass Filter	Using the objectives of enhancing the imperceptibility and robustness as a basis, a robust watermarking approach is developed. Entropy is used to identify the appropriate blocks to embed the watermark	Performance under Salt and Pepper noise, Speckle noise and Rescaling attack is subpar
[29]	Proposed dual image color watermarking for copyright protection against rotation attack. Scramble R, G and B channel using Fibonacci–Lucas transform and Cosine transform-based chaotic system is utilized to encrypt the channels	Combination of graph-based transform and stationary wavelet transform	Noise attacks, filtering attacks, JPEG 2000 compression, Geometric attacks	Proposed scheme is robust against rotation attack and to some extent against scaling and cropping attacks	Scheme does not effectively combat salt and pepper noise
[30]	Copyright protection using fusion domain image watermarking on colored images. It utilizes Arnold transform to encrypt color watermark before embedding	Haar transform and image correction	JPEG compression, JPEG 2000, Cropping, Scaling, Gaussian noise, Salt and Pepper noise, Rotation, Translation, Affine, Shearing	The method is capable of correcting images under different geometric attacks based on the geometric characteristics of the attacked image	It is necessary to fix the size of the watermark and carrier images

Table 1 (continued)

References	Objective	Scheme	Attacks	Findings	Limitation
[8]	A secure watermarking algorithm is developed by combining the sharp frequency localized contourlet transform (SFLCT) and SVD	SVD and sharp frequency localized contourlet transform (SFLCT)	Gaussian noise, Sharpening, Median filter, Weiner filter, Rotation, Shearing, Centre cropping, Salt and Pepper noise, Speckle noise, Scaling, JPEG compression, Translation, Copy attack, First ambiguity attack, Second ambiguity attack	By increasing the dependence of the embedding and detection procedures on the watermark and without adding additional implementations, resistance against ambiguity attacks and the false-positive issue of the SVD-based techniques is improved	Imperceptibility and robustness analysis is presented only for Lena image
[21]	To propose an improved watermarking technique for QR code using States of Matter Search algorithm	DWT and SVD	No attack	To identify appropriate embedding strength factors, two new techniques based on the States of Matter Search (SMS) algorithm are presented	Robustness analysis of proposed technique is not evaluated under various signal processing attacks and common attacks

Table 1 (continued)

References	Objective	Scheme	Attacks	Findings	Limitation
[18]	Proposed an optimized color image watermarking that is reversible and robust	Spiral biogeography-based optimization (SBBO), RDWT, Schur transform (ST)	Gaussian noise, Salt and pepper noise, speckle noise, average filter, median filter, wiener filter, Gaussian LPF, Butterworth LPF, rotation, scaling, cropping, translate, cutting, shear, histogram equalization, gamma correction, sharpening, JPEG compression,	Scheme is shift-invariant, has a high embedding capacity and is computationally fast due to the hybridization of redundant discrete wavelet transform and Schur transform	The proposed approach does not perform well when subjected to Gaussian noise
[23]	For color images, a dual watermarking method with high embedding capacity has been developed using the SWT and SVD features	SWT, SVD and genetic algorithm (GA)	Gaussian noise, salt and pepper noise, median filtering, scaling, rotation, blur, JPEG compression, cropping, sharpen, histogram equalization, brighten, darken, hybrid of geometric attacks	The genetic algorithm is used to optimize the proposed scheme for the optimal trade-off between imperceptibility and robustness	Rotation, sharpening and histogram equalization attacks are difficult for the scheme to successfully resist off

Table 1 (continued)

References	Objective	Scheme	Attacks	Findings	Limitation
[11]	The robust and fragile watermarks are two watermarks that are implanted in the medical image as part of the proposed multifunctional watermarking to achieve privacy control and prevent tampering with sensitive data	RDWT and QR decomposition	Scaling, averaging, rotation, cropping, JPEG compression, Gaussian noise, salt and pepper noise, speckle noise, histogram equalization, unsharp masking, tampering attacks, collage attacks, counterfeiting attack, content only tampering	The performance of robust watermarking was improved by using the Particle Swarm Bacterial Foraging Optimization (PSBFO) technique to choose the threshold value for achieving the best outcomes in terms of transparency and attack resistance	Computational complexity of proposed scheme is not discussed
[31]	A blind, secure and robust image watermarking method based on redundant discrete wavelet transform (RDWT) and Non-Subsampled Contourlet Transform (NSCT) is proposed	Non-subsampled contourlet transform (NSCT) and RDWT	Motion blur, sharpening, JPEG compression, histogram equalization, median filter, Gaussian low-pass filter, speckle noise, salt and pepper noise, Gaussian noise	This method inserts a watermark into the cover image's wavelet sub-band of contourlet sub-band in order to enable blind extraction	Analysis of the computational complexity of the proposed scheme is not provided

Table 1 (continued)

References	Objective	Scheme	Attacks	Findings	Limitation
[32]	Singular Value Decomposition Ghost Imaging (SVDGI)-based optical image watermarking is proposed. Encryption of watermark is performed with the help of SVDGI and then embedding is done using transforms	DCT and LWT	Gaussian noise, salt and pepper noise, cropping, JPEG compression	Optical experiment and simulation results show good performance in terms of imperceptibility and robustness against different attacks	Robustness analysis of proposed scheme is tested only against few attacks
[14]	Hybrid image watermarking based on LWT-DCT-SVD. Security is provided by message digest hash algorithm	LWT-DCT-SVD	Salt and pepper noise, JPEG compression, Gaussian noise, speckle noise, median filter, average filter, rotation, histogram equalization	Dual watermarks provide security, and it also conserves transmission bandwidth	Performance under Salt and pepper noise, speckle noise and rotation is not satisfactory
[15]	For secure medical image transfer, watermarking approach is presented	DWT and SVD	Filtering attacks, noise attacks, lossy compression, geometric attacks	Singular values get modified by substitution process with integration of watermark bits	X-ray images are more suited for the proposed approach
[16]	Proposed blind watermarking strategy for protecting medical images. Singular matrix coefficients are integrated with the watermark bits	DWT and SVD	Salt and pepper noise, Gaussian noise, rotation, speckle noise, JPEG compression, average filter, cropping, resizing, histogram equalization, gamma correction, sharpening, scaling	A strategy to guarantee the accuracy of retinal images is presented. The watermark made up of patient data makes it possible to verify both the patient and the information linked to the image's capture	DWT lacks the translation-invariance property

(3) RSVD is used in place of SVD as computational complexity of RSVD is less. SVD requires more memory spaces in comparison with RSVD. SVD is also cost inefficient mechanism.
(4) Henon encryption is used to secure the watermark images. The proposed watermarking method is free from false-positive problem.
(5) Dual watermarks are used to further enhance the security of the presented work.
(6) Scaling factor plays an important role in optimizing robustness, imperceptibility, and capacity. So, to get the optimum scaling factor a novel fitness function is used and optimized value is obtained by applying MRFO.

Rest of the paper is organized in six sections. Preliminaries are discussed in Sect. 2. Watermark embedding and extraction processes are presented in Sect. 3. Quality metrics used to evaluate the performance of the proposed scheme is mentioned in Sect. 4. Section 5 presents the simulation results in terms of imperceptibility, robustness, computational complexity, capacity and security. Comparison with existing techniques is presented in Sect. 6, while conclusion of proposed method is drawn in Sect. 7.

2 Preliminaries

2.1 Conversion of Color Spaces

For ‘real world’ images, RGB is the most popular color model. Nevertheless, the RGB color model is ineffective when dealing with actual image processing (such as modifying an image’s color or intensity). To tackle these kinds of image processing applications, the YCbCr color space was developed along with several other color models [10]. Compared to RGB color space, YCbCr is more resistant to attacks. YCbCr color is obtained from RGB color space using Eq. (1):

$$\begin{bmatrix} Y \\ Cb \\ Cr \end{bmatrix} = \begin{bmatrix} 0.2990.5870.114 \\ -0.169-0.3310.500 \\ 0.500-0.419-0.081 \end{bmatrix} \times \begin{bmatrix} R \\ G \\ B \end{bmatrix} + \begin{bmatrix} 0 \\ 128 \\ 128 \end{bmatrix} \tag{1}$$

RGB color is converted from YCbCr color space using Eq. (2):

$$\begin{bmatrix} R \\ G \\ B \end{bmatrix} = \begin{bmatrix} 1.00-0.001.40 \\ 1.00-0.34-0.71 \\ 1.001.770.00 \end{bmatrix} \times \begin{bmatrix} Y \\ Cb-128 \\ Cr-128 \end{bmatrix} \tag{2}$$

2.2 Redundant Discrete Wavelet Transform

The DWT decomposes the signal into coarse coefficients and detail coefficients in order to analyze a digital image at various frequency bands with various resolutions. DWT utilizes high-pass filter and low-pass filter with down-sampling along rows and columns of an image to decompose it into sub-bands. This down-sampling procedure may remove image details that could be valuable but are not necessary to replicate the image. The loss of coefficients due to down-sampling, alters the image slightly and decreases the probability of reproduction of the image. To overcome DWT's shift-variant property, researchers have proposed RDWT which is shift-invariant [4]. By forgoing down-sampling and up-sampling, RDWT solves the shift variance issue with DWT and boosts embedding capacity.

2.3 Randomized Singular Value Decomposition

The concept of approximation matrix factorization utilizing random projections is explored by the advanced form of SVD known as RSVD [33]. RSVD of a matrix X is given as:

$$X_k = \hat{U}\hat{\Sigma}\hat{V}^T \tag{3}$$

In Eq. (3), $\hat{U}$ and $\hat{V}$ are orthonormal matrices, k is target rank, and $\hat{\Sigma}$ is diagonal matrix whose diagonal elements represent singular values.

There are two stages to the RSVD method. The first stage involves random sampling to produce a reduced matrix whose range is approximation of the range of the input matrix X. By employing the randomization strategy in this stage, a nearly optimal basis matrix A is obtained. By projecting X to low-dimensional space, we can obtain another matrix Z as shown in Eq. (4):

$$Z = A^T X \tag{4}$$

In the second stage, the reduced matrix is factorized by taking SVD of Z.

$$Z = \tilde{U}\Sigma V^T \tag{5}$$

In Eq. (5), $\tilde{U}$ is approximation of left singular matrix $\hat{U}$.

2.4 Henon Mapping

Classical dynamic system in discrete time domain was proposed by Henon [34]. A point (x_i, y_i) transforms into (x_{i+1}, y_{i+1}) using Henon mapping as shown in Eq. (6):

$$\begin{cases} x_{i+1} = 1 - ax_i^2 + y_i \\ y_{i+1} = bx_i \end{cases} \tag{6}$$

The Henon mapping can be seen to be a chaotic map made up of the variables x and y, where a and b are Henon map parameters. Henon map can produce confusion and histogram uniformity for image encryption. Henon map has near-optimal randomization characteristics and is computationally effective [35]. For Henon map encryption, control parameters 'a' and 'b' play an important role. Suitable values of control parameters generate the encrypted image which appears meaningless and we cannot decipher any information of original image. Here, $a = 1.4$ and $b = 0.34$ are chosen for encrypting the images.

2.5 Manta Ray Foraging Optimization

MRFO is a metaheuristic optimization [3, 5] technique that draws inspiration from the manta rays' intelligent foraging patterns [36]. Manta rays utilize three foraging strategies, notably the chain, cyclone and somersault, to search for food. In order to find a globally optimal solution to the problem, the MRFO algorithm imitates these foraging strategies.

2.5.1 Chain Foraging

Manta rays establish a foraging chain by forming a line with their heads and tails. A larger concentration of plankton, which is the main food source for manta rays, is considered by MRFO as the best solution. Manta ray update their position iteratively with respect to the manta rays in front of it and the best solution obtained so far. The chain foraging mathematical model is explained in Eq. (7):

$$p_i^{t+1} = \begin{cases} p_i^t + r_1 \cdot \left(p_{best}^t - p_i^t\right) + \alpha \cdot \left(p_{best}^t - p_i^t\right) & i = 1 \\ p_i^t + r_2 \cdot \left(p_{i-1}^t - p_i^t\right) + \alpha \cdot \left(p_{best}^t - p_i^t\right) & i = 2, 3, ..., N_{pop} \end{cases} \tag{7}$$

where p_i^t is the individual's position at time 't', p_{best}^t is the best position, N_{pop} represents the population size, $\alpha = 2 \cdot r_3 \cdot \sqrt{\log(r_4)}$ is the weight coefficient, and $r_i \in [0, 1] i = 1, 2, 3, 4$ are random values.

2.5.2 Cyclone Foraging

Manta rays spiral toward them after finding where their food supply is and reposition themselves to be in that area, which is the best location so far. Mathematically, cyclone foraging formulated as shown in Eq. (8):

$$p_i^{t+1} = \begin{cases} p_{best}^t + r_5 \cdot \left(p_{best}^t - p_i^t\right) + \beta \cdot \left(p_{best}^t - p_i^t\right) & i = 1 \\ p_{best}^t + r_6 \cdot \left(p_{i-1}^t - p_i^t\right) + \beta \cdot \left(p_{best}^t - p_i^t\right) & i = 2, 3, \ldots, N_{pop} \end{cases} \tag{8}$$

$$\beta = 2 \cdot \exp\left(r_7 \cdot \frac{(iter_{\max} - iter + 1)}{iter_{\max}}\right) \cdot \sin(2\pi r_7) \tag{9}$$

In Eq. (9), $iter_{max}$ and $iter$ are maximum iteration and current iteration, respectively, $r_i \in [0, 1] i = 5, 6, 7$ are random values, and β is weight coefficient.

In order to fully utilize the region around food, spiral foraging primarily uses food as a reference point. Manta rays will randomly begin searching for different areas with higher densities of planktons if they see low-density planktons. It can be mathematically expressed as shown in Eq. (11):

$$p_{rand} = lb + r_8 \cdot (ub - lb) \tag{10}$$

$$p_i^{t+1} = \begin{cases} p_{rand} + r_9 \cdot \left(p_{best}^t - p_i^t\right) + \beta \cdot \left(p_{best}^t - p_i^t\right) & i = 1 \\ p_{rand} + r_{10} \cdot \left(p_{i-1}^t - p_i^t\right) + \beta \cdot \left(p_{best}^t - p_i^t\right) & i = 2, 3, \ldots, N_{pop} \end{cases} \quad (11)$$

lb and ub are lower and upper bounds of search region, p_{rand} is random position in the search region and given by Eq. (10), and $r_i \in [0, 1] i = 8, 9, 10$ are uniformly distributed random values.

Hence, the behavior of the cyclones helps in MRFO exploration and exploitation.

2.5.3 Somersault Foraging

In somersault strategy, to get closer to the location of the meal, Manta rays somersault around it and update their position around the best pivot point obtained thus far. Mathematical model of somersault foraging strategy is expressed by Eq. (12):

$$p_i^{t+1} = p_i^t + S \cdot \left(r_{11} \cdot p_{best}^t - r_{12} \cdot p_i^t\right) \quad i = 1, 2, 3, \ldots, N_{pop} \quad (12)$$

where S is somersault factor, and $r_i \in [0, 1] i = 11, 12$.

The two control factors that must be carefully adjusted to ensure the MRFO performs well are the population size (N_{pop}) and the maximum number of iterations ($iter_{max}$).

3 Proposed Methodology

In this section, an optimized dual watermarking technique based on RDWT-RSVD-MRFO and encryption using Henon mapping is introduced. RGB color space of cover image is converted into YCbCr color space, and luminance component is further utilized to embed dual watermarks. 3-level RDWT applied on luminance component of cover image and LH, HL sub-bands is further processed with RSVD. 1-level RDWT applied on both watermarks and before performing RSVD on their sub-bands, LH and HL sub-bands, is encrypted using Henon mapping. Singular values of two sub-bands of cover image are modified by utilizing singular values of watermarks with suitable strength factor. The strength factor utilized to embed watermarks is optimized using MRFO technique. To generate watermarked image, inverse RSVD and inverse RDWT are applied and converted back into RGB color space. For watermark extraction, inverse process of embedding is followed. Embedding and extraction procedure of proposed scheme is shown in Figs. 1 and 2.

3.1 Embedding Procedure

Detailed watermark embedding procedure to embed a grayscale image and a text image watermark is listed below:

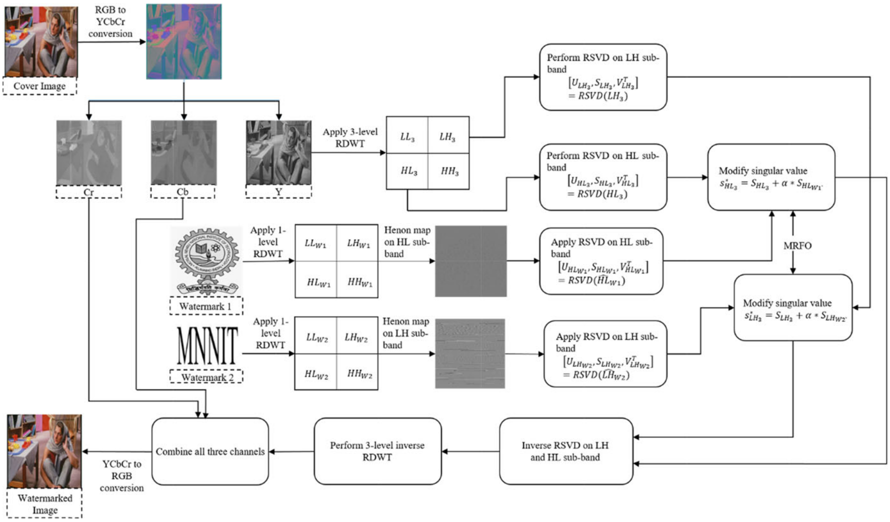

Fig. 1 Watermark embedding process block diagram

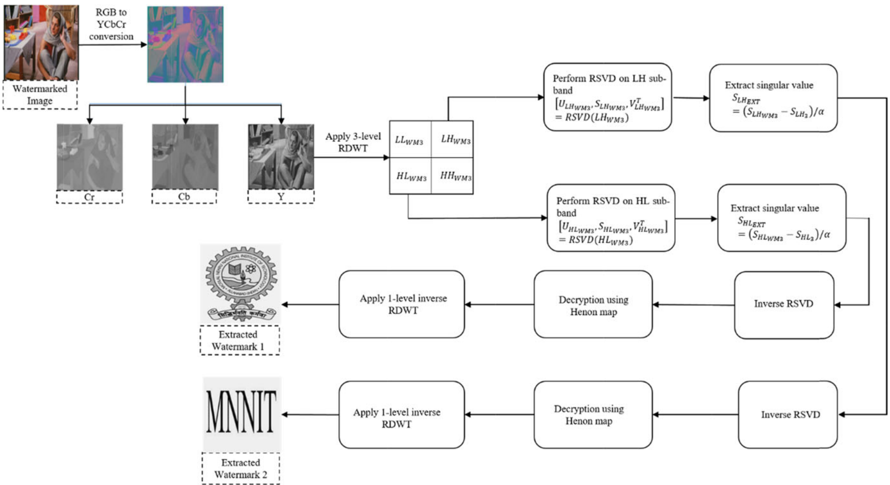

Fig. 2 Extraction process of proposed watermarking scheme

1. Convert the RGB cover image into YCbCr color space as expressed in Eq. (13):

$$[cover\_img_Y, cover\_img_{Cb}, cover\_img_{Cr}] \leftarrow RGBtoYCbCr(cover\_img) \tag{13}$$

2. Perform 1-level RDWT on luminance component to divide it into four sub-bands as shown in Eq. (14):

$$[LL_1, LH_1, HL_1, HH_1] \leftarrow RDWT(cover\_img_Y) \tag{14}$$

3. LL_1 sub-band of luminance component which is obtained from above step is again processed with 2-level RDWT which decomposes it into several sub-bands as expressed in Eqs. (15) & (16):

$$[LL_2, LH_2, HL_2, HH_2] \leftarrow RDWT(LL_1) \tag{15}$$

$$[LL_3, LH_3, HL_3, HH_3] \leftarrow RDWT(LL_2) \tag{16}$$

4. HL_3 and LH_3 sub-bands generated after 3-level RDWT are utilized to embed both watermarks. RSVD is applied on both sub-bands to decompose it into three matrices as shown in Eqs. (17) and (18):

$$\left[U_{HL_3}, S_{HL_3}, V_{HL_3}^T\right] \leftarrow RSVD(HL_3) \tag{17}$$

$$\left[U_{LH_3}, S_{LH_3}, V_{LH_3}^T\right] \leftarrow RSVD(LH_3) \tag{18}$$

5. Consider grayscale image and a text image as watermark and 1-level RDWT is applied on both watermarks as expressed in Eqs. (19) and (20) to divide it into four sub-bands.

$$[LL_{W1}, LH_{W1}, HL_{W1}, HH_{W1}] \leftarrow RDWT(watermark\_1) \tag{19}$$

$$[LL_{W2}, LH_{W2}, HL_{W2}, HH_{W2}] \leftarrow RDWT(watermark\_2) \tag{20}$$

6. Select HL_{W1} of first watermark and perform Henon mapping on the band to encrypt this sub-band expressed as Eq. (21):

$$\widehat{HL}_{W1} \leftarrow henon\_map\_enc(HL_{W1}) \tag{21}$$

7. Encrypt LH_{W2} of second watermark using Henon mapping shown in Eq. (22) on this sub-band.

$$\widehat{LH}_{W2} \leftarrow henon\_map\_enc(LH_{W2}) \tag{22}$$

8. Decompose encrypted $\widehat{HL}_{W1}$ and $\widehat{LH}_{W2}$ into three sub matrices by applying RSVD on it as expressed in Eqs. (23) and (24):

$$\left[U_{HL_{W1}}, S_{HL_{W1}}, V_{HL_{W1}}^T\right] \leftarrow RSVD\left(\widehat{HL}_{W1}\right) \tag{23}$$

$$\left[U_{LH_{W2}}, S_{LH_{W2}}, V_{LH_{W2}}^{T}\right] \leftarrow RSVD\left(\widehat{LH}_{W2}\right) \tag{24}$$

9. To embed first watermark into HL_3 of cover image, modify the singular value of HL_3 by multiplying strength factor 'α' obtained by MRFO with singular value of $\widehat{HL}_{W1}$ shown in Eq. (25):

$$S_{HL_3}^{*} = S_{HL_3} + \alpha * S_{HL_{W1}} \tag{25}$$

10. LH_3 of cover image is selected to embed the second watermark. Optimized strength factor 'α' multiplied with singular value of $\widehat{LH}_{W2}$, and the product is added with singular value of LH_3 expressed as Eq. (26):

$$S_{LH_3}^{*} = S_{LH_3} + \alpha * S_{LH_{W2}} \tag{26}$$

11. Perform inverse RSVD to rebuild the sub-bands HL_3 and LH_3 after modification of their singular values as mentioned in Eqs. (27) and (28):

$$HL_3^{*} \leftarrow IRSVD\left(U_{HL_3}, S_{HL_3}^{*}, V_{HL_3}^{T}\right) \tag{27}$$

$$LH_3^{*} \leftarrow IRSVD\left(U_{LH_3}, S_{LH_3}^{*}, V_{LH_3}^{T}\right) \tag{28}$$

12. Apply 3-level inverse RDWT to get back luminance component of watermarked image expressed as Eq. (29):

$$watermarked_Y \leftarrow IRDWT\left(LL_3, LH_3^{*}, HL_3^{*}, HH_3\right) \tag{29}$$

13. Combine chrominance and luminance components to generate the watermarked image as mentioned in Eq. (30):

$$watermarked\_img_{YCbCr} \leftarrow combine(watermarked_Y, cover\_img_{Cb}, cover\_img_{Cr}) \tag{30}$$

14. Convert YCbCr color space into RGB color space to get the final watermarked image as shown in Eq. (31):

$$watermarked\_img_{RGB} \leftarrow watermarked\_img_{YCbCr} \tag{31}$$

3.2 Extraction Procedure

To extract the embedded watermarks from the watermarked image, reverse process of embedding procedure is followed. Steps involved in extraction of watermarks are listed below:

1. Conversion of received color watermarked image into YCbCr color space shown in Eq. (32):

$$(watermarked\_img_Y, watermarked\_img_{Cb}, watermarked\_img_{Cr}) \leftarrow RGBtoYCbCr(watermarked\_img) \tag{32}$$

2. Further, perform 3-level RDWT on luminance component of watermarked image as expressed in Eq. (33) to decompose it into several sub-bands:

$$[LL_{WM3}, LH_{WM3}, HL_{WM3}, HH_{WM3}] \leftarrow RDWT(watermarked\_img_Y) \tag{33}$$

3. To extract the embedded watermarks from received watermarked image, apply RSVD on LH_{WM3} and HL_{WM3} to decompose it into three matrices expressed as Eqs. (34) and (35):

$$\left[U_{HL_{WM3}}, S_{HL_{WM3}}, V^T_{HL_{WM3}}\right] \leftarrow RSVD(HL_{WM3}) \tag{34}$$

$$\left[U_{LH_{WM3}}, S_{LH_{WM3}}, V^T_{LH_{WM3}}\right] \leftarrow RSVD(LH_{WM3}) \tag{35}$$

4. Extract singular value of *HL* sub-band by using $S_{HL_{WM3}}$, S_{HL_3} and strength factor 'α' using Eq. (36):

$$S_{HL_{EXT}} \leftarrow \left(S_{HL_{WM3}} - S_{HL_3}\right)/\alpha \tag{36}$$

5. By using $S_{LH_{WM3}}$, strength factor 'α' and S_{LH_3}, extract LH sub-band singular value as expressed in Eq. (37):

$$S_{LH_{EXT}} \leftarrow \left(S_{LH_{WM3}} - S_{LH_3}\right)/\alpha \tag{37}$$

6. Perform inverse RSVD to rebuild sub-bands by utilizing corresponding extracted singular values using Eqs. (38) and (39):

$$HL_{EXT} \leftarrow IRSVD\left(U_{HL_{W1}}, S_{HL_{EXT}}, V^T_{HL_{W1}}\right) \tag{38}$$

$$LH_{EXT} \leftarrow IRSVD\left(U_{LH_{W2}}, S_{LH_{EXT}}, V^T_{LH_{W2}}\right) \tag{39}$$

7. Decrypt both extracted sub-bands using Henon mapping as shown in Eqs. (40) and (41):

$$\widehat{HL}_{EXT} \leftarrow henon\_map\_dec(HL_{EXT}) \tag{40}$$

$$\widehat{LH}_{EXT} \leftarrow henon\_map\_dec(LH_{EXT}) \tag{41}$$

8. Apply 1-level inverse RDWT to extract first watermark by using Eq. (42):

$$extracted\_watermark_1 \leftarrow IRDWT\left(LL_{W1}, LH_{W1}, \widehat{HL}_{EXT}, HH_{W1}\right) \quad (42)$$

9. Extract second watermark by applying 1-level inverse RDWT as expressed in Eq. (43):

$$extracted\_watermark_2 \leftarrow IRDWT\left(LL_{W2}, \widehat{LH}_{EXT}, HL_{W2}, HH_{W2}\right) \quad (43)$$

3.3 Optimization Procedure for Image Watermarking using MRFO

The strength factor has a significant impact on the watermarking scheme's visual quality and robustness. A minor decrease in the value of strength factor improves the watermarked image's perceptual quality, but significantly degrades the recovered watermark image quality. Similarly, when the strength factor has a high value, the visual quality degrades but the robustness is improved. Consequently, it is essential to find the appropriate strength factor value that makes a compromise between invisibility and robustness for embedding with singular values. To provide the highest level of visual quality and robustness for each image, a different strength factor value is required. The issue of determining the ideal strength factor to avoid the conflict between invisibility and robustness can also be resolved by employing bio-inspired optimization techniques. In this paper, optimized strength factor is calculated using MRFO technique to modify the singular values of sub-bands of cover image using singular value of watermark's sub-band.

A single objective function-based MRFO is employed in the optimization process of the proposed watermarking technique to determine the strength factor. For each iteration of the MRFO, the strength factor value is analyzed after applying various attacks. To create the suitable fitness function, the robustness of the watermarked image and its visual quality should be assessed. Objective function of proposed scheme of watermarking is defined in Eq. (44):

$$obj\_fun = \frac{PSNR}{100} + \frac{1}{\left(\sum_{i=1}^{k} NC_{1i} + \sum_{i=1}^{k} NC_{2i}\right)} + \left(-\left(\frac{KLDIV + JSDIV + BER}{3}\right)\right) \quad (44)$$

where k is the total number of attacks applied on watermarked image.

Upper bound range and lower bound range of PSNR [Eq. (45)], NC [Eq. (46)], KL DIV [Eq. (47)], JS DIV [Eq. (48)] and BER [Eq. (49)] are mentioned below:

$$55 \leq PSNR \leq 65 \quad (45)$$

$$0.9 \leq NC_1, \quad NC_2 \leq 1 \tag{46}$$

$$1.2\exp(-06) \leq \text{KL DIV} \leq 1.7\exp(-05) \tag{47}$$

$$3.2\exp(-07) \leq JSDIV \leq 2.6\exp(-06) \tag{48}$$

$$0 \leq BER \leq 0.6 \tag{49}$$

Several attacks are considered for watermarked image to calculate the optimal strength factor using MRFO. Steps followed during MRFO to obtain strength factor are described below.

1. Initialize the somersault factor (S), total number of population (N_{pop}), maximum number of iteration ($iter_{max}$).
2. Define the objective function of optimization problem and range of variables.
3. Randomly initialize Manta ray position and find best solution by calculating objective function.
4. Start the loop for $i = 1 : N_{pop}$, till the end.
5. Estimate the fitness value and update the Manta ray position according to it.
6. If $Rand > 0.5$, cyclone foraging strategy is performed.
   If $\frac{iter}{iter_{max}} < Rand$, update the Manta ray position according to Eq. (11)
   else update the Manta ray position according to Eq. (8)
7. If $Rand < 0.5$, chain foraging strategy is applied and Manta ray position is updated according to Eq. (7)
8. Calculate the objective function and update the best position obtained so far.
9. Perform somersault foraging and update the position according to Eq. (12).
10. If stopping criteria is satisfied, select the best solution among all; otherwise, repeat steps (5)–(10).

In the proposed scheme, strength factor is calculated by considering $N_{pop} = 10$, $iter_{max} = 50$, S = 2, and lower and upper bound as according to Eqs. (45)–(49). Flowchart of the MRFO to obtain an optimized scaling factor for proposed scheme is shown in Fig. 3.

4 Quality Metrics

To evaluate the performance of proposed technique, quality metrics used here are PSNR, SSIM, NC, BER and two new imperceptibility parameters KL DIV, JS DIV. PSNR, SSIM, KL DIV and JS DIV are used to measure imperceptibility, whereas NC and BER are used to evaluate robustness of proposed algorithm. Invisibility of an embedded watermark in watermarked image is known as imperceptibility. Embedded watermark must be invisible so that human eye cannot distinguish between cover image and watermarked image. Different parameters to assess imperceptibility of watermarking schemes are available in the literature. Robustness is defined as the resistance against attacks or modifications.

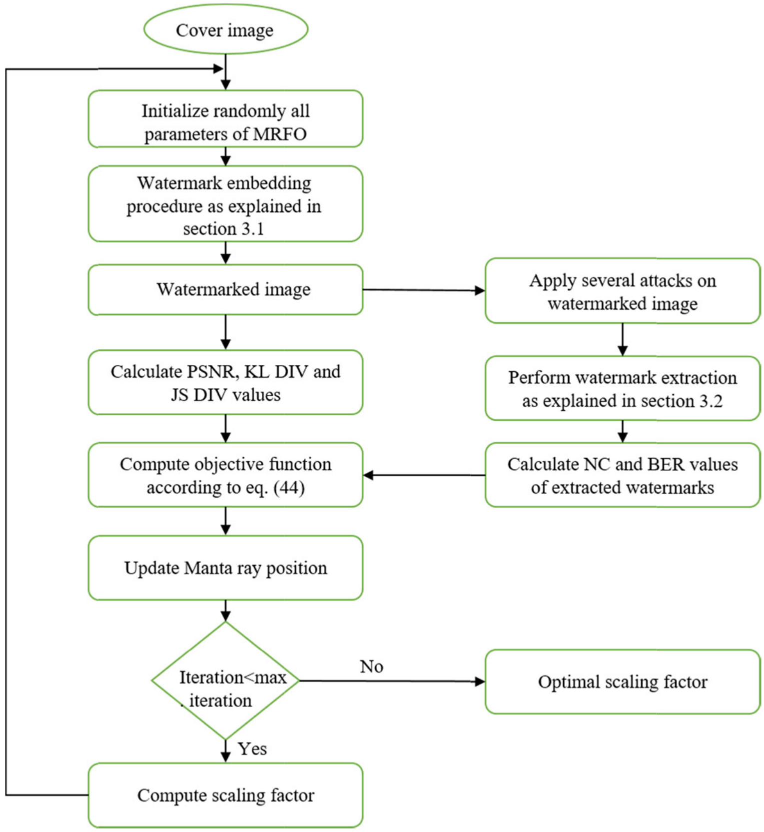

Fig. 3 Flowchart of MRFO to obtain an optimized scaling factor for the proposed scheme

PSNR: one of the most common parameters to evaluate imperceptibility is PSNR. It is calculated between cover image and watermarked image. Mathematically, PSNR can be expressed as given by Eq. (50) and is calculated in decibel:

$$PSNR(cov\_img, wmarked\_img) = 10 \times log_{10}\left[\frac{3 \times 255^2}{mse_R + mse_G + mse_B}\right] \quad (50)$$

where mse is mean square error and is calculated using Eq. (51) between watermarked image and cover image. The width and height of both images are denoted by M and N:

$$mse(cov\_img, wmarked\_img) = \frac{1}{M \times N}\sum_{x=1}^{M}\sum_{y=1}^{N}(cov\_img - wmarked\_img)^2 \quad (51)$$

SSIM: it is a metric for comparing the similarity of two images. Instead of focusing on a pixel-by-pixel difference, SSIM aims to evaluate the structural similarity between the two images. It is expressed as Eq. (52):

$$SSIM = \frac{\left(2\mu_{cov\_img}\mu_{wmarked\_img} + C_1\right)\left(2\sigma_{cov\_img,wmarked\_img} + C_2\right)}{\left(\mu^2_{cov\_img} + \mu^2_{wmarked\_img} + C_1\right)\left(\sigma^2_{cov\_img} + \sigma^2_{wmarked\_img} + C_2\right)} \tag{52}$$

where μ_{cov_img} is average of cover image, $\mu_{wmarked\_img}$ is average of watermarked image, $\sigma_{cov\_img,wmarked\_img}$ is covariance of watermarked image and cover image, $\sigma^2_{cov\_img}$ is variance of cover image, $\sigma^2_{wmarked\_img}$ is variance of watermarked image, and C_1 and C_2 are constants.

KL DIV: the distance between the cover and watermarked signal's histograms is calculated using KL divergence. It can be calculated using Eq. (53):

$$KLDiv(cover, watermarked) = \int p_{watermarked}(x) log \frac{p_{watermarked}(x)}{p_{cover}(x)} dx \tag{53}$$

where $p_{watermarked}$ and p_{cover} are probability of watermarked signal and cover signal respectively [13].

JS DIV: by extending KL divergence, JS divergence determines a symmetrical score and distance between two probability distributions. Mathematically, it can be expressed as Eq. (54):

$$JSDiv(x, y) = \frac{1}{2} KLDiv(x, p) + \frac{1}{2} KLDiv(p, y) \tag{54}$$

where $p = \frac{1}{2} \times (x + y)$.

To evaluate robustness of watermarking technique, parameters NC and BER are utilized. NC and BER are calculated between original watermark and extracted watermark.

NC: the correlation between the extracted watermark image and the original watermark image is measured by NC. The NC value ranges from -1 to 1. If the extracted watermark image is nearly identical to the original watermark image, the correlation value will be close to 1, whereas a correlation value of -1 indicates that the extracted watermark image is negative to the original watermark image. NC is given by Eq. (55):

$$NC = \frac{\sum_{x=1}^{M}\sum_{y=1}^{N}(wmark - \mu_{wmark}) \times \left(ext\_wmark - \mu_{ext\_wmark}\right)}{\sqrt{\sum_{x=1}^{M}\sum_{y=1}^{N}(wmark - \mu_{wmark})^2} \times \sqrt{\sum_{x=1}^{M}\sum_{y=1}^{N}\left(ext\_wmark - \mu_{ext\_wmark}\right)^2}} \tag{55}$$

where μ_{wmark} is the mean of original watermark and μ_{ext_wmark} is the mean of extracted watermark.

BER: BER is the ratio of number of error bits to the total number of transmitted bits. Mathematically, it can be expressed as Eq. (56):

$$BER = \frac{Number\ of\ error\ bits}{Total\ number\ of\ transmitted\ bits} \tag{56}$$

5 Simulation Results and Discussion

Evaluation of proposed scheme is performed using MATLAB software. Performance of proposed technique is evaluated using various test images of size 512 × 512 which includes medical and non-medical images. Medical images include Brain CT Scan, Fundus, Ultrasound and X-Ray. Non-medical images include Airplane, Barbara, Goldhill, Mandrill, Pepper, Sailboat and Zelda images. MNNIT logo and MNNIT text watermark grayscale images of size 512 × 512 are used as watermarks. Before embedding, both watermarks are encrypted using Henon mapping and these encrypted images are then embedded in cover image. NC values are calculated for both extracted watermarks, while BER is measured only for text watermark. Imperceptibility analysis, robustness analysis along with capacity analysis, computational complexity and security analysis of proposed technique is discussed below. Simulation results of presented scheme are also compared with some existing state-of-the-art schemes.

5.1 Imperceptibility Analysis

To measure the imperceptibility of proposed method, parameters PSNR, SSIM, KL DIV and JS DIV are utilized. Table 2 shows the corresponding cover images with watermarked images and extracted watermarks. PSNR, SSIM, NC for all twelve test images under no attack are shown in Table 2. If PSNR and SSIM values are more than 30 dB and 0.90, respectively, the watermarking approach is considered to have better imperceptibly [18]. It is clear from Table 2 that proposed scheme attains PSNR above 60 dB for all cover images and SSIM above 0.99 which shows the presented technique provides better imperceptibility in terms of PSNR and SSIM. KL DIV and JS DIV are listed in Tables 4 and 5 for eight test images. Minimum KL DIV value of 2.57×10^{-6} and minimum JS DIV value of 6.42×10^{-7} are achieved for Barbara image without attacks. NC values for all extracted watermarks are above 0.99 without attacks which show that the extracted watermarks and original watermarks are almost similar. Lowest attained BER value is 0.59% for Goldhill image, and highest BER value is 0.61 for ultrasound 1 image under no attacks.

5.2 Robustness Analysis

To assess the robustness of proposed scheme, various noise attacks, filtering attacks, geometric attacks are applied on all test images. Twenty-two attacks are utilized for robustness analysis such as Gaussian noise (var = 0.01), salt and pepper noise (0.01),

Table 2 Watermarked images with corresponding PSNR and SSIM values and their respective extracted watermarks with NC values under no attack

Images	Cover image	Watermarked image	Extracted Watermark 1	Extracted Watermark 2
Airplane		 PSNR = 60.58 SSIM = 0.9998	 NC = 0.9999	 NC = 0.9998
Barbara		 PSNR = 61.11 SSIM = 0.9999	 NC = 0.9999	 NC = 0.9998
Brain CT Scan	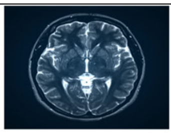	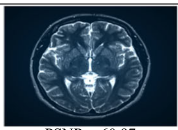 PSNR = 60.97 SSIM = 0.9999	 NC = 0.9999	 NC = 0.9998
Fundus	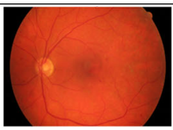	 PSNR = 61.10 SSIM = 0.9995	 NC = 0.9999	 NC = 0.9998
Goldhill		 PSNR = 60.15 SSIM = 0.9998	 NC = 0.9999	 NC = 0.9998
Mandrill	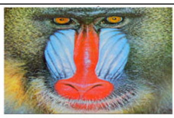	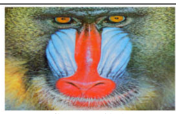 PSNR = 60.15 SSIM = 0.9999	 NC = 0.9998	 NC = 0.9998
Peppers		 PSNR = 60.71 SSIM = 0.9998	 NC = 0.99999	 NC = 0.9998
Sailboat		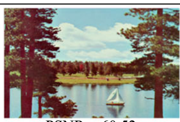 PSNR = 60.52 SSIM = 0.9999	 NC = 0.9999	 NC = 0.9998

Table 2 (continued)

Images	Cover image	Watermarked image	Extracted Watermark 1	Extracted Watermark 2
Ultrasound 1		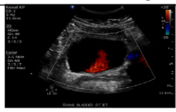 PSNR = 61.43 SSIM = 0.9999	 NC = 0.9999	 NC = 0.9998
Ultrasound 2	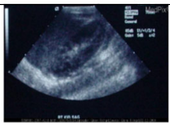	 PSNR = 60.76 SSIM = 0.9998	 NC = 0.9999	 NC = 0.9998
X-ray		 PSNR = 60.56 SSIM = 0.9998	 NC = 0.9999	 NC = 0.9998
Zelda		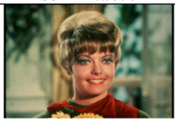 PSNR = 60.63 SSIM = 0.9998	 NC = 0.9999	 NC = 0.9998
Average of 100 images [40]	PSNR = 60.57, SSIM = 0.9998 KL DIV = 3.62×10^{-6}, JS DIV = 10.48×10^{-7} NC1 = 0.9999, NC2 = 0.9998, BER = 0.60			

speckle noise (var = 0.01), median filter (3 × 3), Gaussian low-pass filter {(3 × 3), (5 × 5)}, average filter {(3 × 3), (5 × 5)}, Poisson noise, rotation (30°, 60°), horizontal flipping, vertical flipping, histogram equalization, JPEG compression (QF = 10, 50, 90), JPEG 2000 (CR = 12), sharpening, shearing, motion blur and Gamma correction. Attacked watermarked images and its corresponding watermarks are shown only for Barbara image. Table 3 shows the Barbara image when subjected to different attacks and its corresponding extracted watermarks. It is evident from Table 3 that proposed scheme is able to withstand various attacks and embedded watermarks are extracted successfully.

Imperceptibility and robustness analysis considered under different noises and attacks are shown in Figs. 4, 5, 6, 7, 8, 9, 10 and 11 for all cover images. PSNR of all cover images is calculated by considering different attacks and shown in Figs. 4, 5, 6 and 7. It is clear from these figures that PSNR value is above 25 dB under most of the attacks such as median filter, salt and pepper noise, Gaussian noise, Poisson noise, speckle noise, Gaussian low-pass filter, average filter, sharpening, JPEG compression and Gamma correction.

For filter attacks, maximum attained PSNR value is 51.89 dB for Fundus image under Gaussian low-pass filter (3 × 3) and minimum value of PSNR 26.40 dB for Barbara image under average filter (5 × 5) attack. In case of noise attacks, highest obtained PSNR value is 61.43 dB for Ultrasound 1 image under Poisson noise and

Table 3 Barbara image and corresponding extracted watermarks under various attacks

Attacks	Cover Image	Attacked Image	Extracted Watermark 1	Extracted Watermark 2
No Attack				MNNIT
Median Filter (3×3)				MNNIT
Salt & Pepper (0.01)				MNNIT
Gaussian Noise (var = 0.01)				MNNIT
Poisson Noise				MNNIT
Speckle Noise (var = 0.01)				MNNIT
Gaussian LPF (3×3)				MNNIT
Gaussian LPF (5×5)				MNNIT
Average Filter (3×3)				MNNIT
Average Filter (5×5)		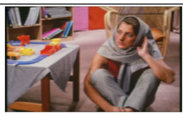		MNNIT
Rotation (30°)				MNNIT

Table 3 (continued)

Attacks	Cover Image	Attacked Image	Extracted Watermark 1	Extracted Watermark 2
Rotation (60°)				
Vertical Flipping				
Horizontal Flipping				
Histogram Equalization				
Sharpening				
JPEG Compression (QF = 10)				
JPEG Compression (QF = 50)				
JPEG Compression (QF = 90)				
JPEG 2000 (CR = 12)				
Motion Blur (45, 45)				
Shearing	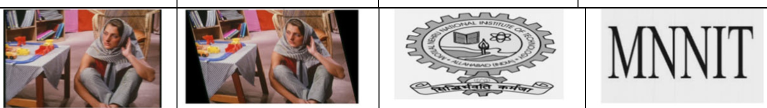			
Gamma Correction				

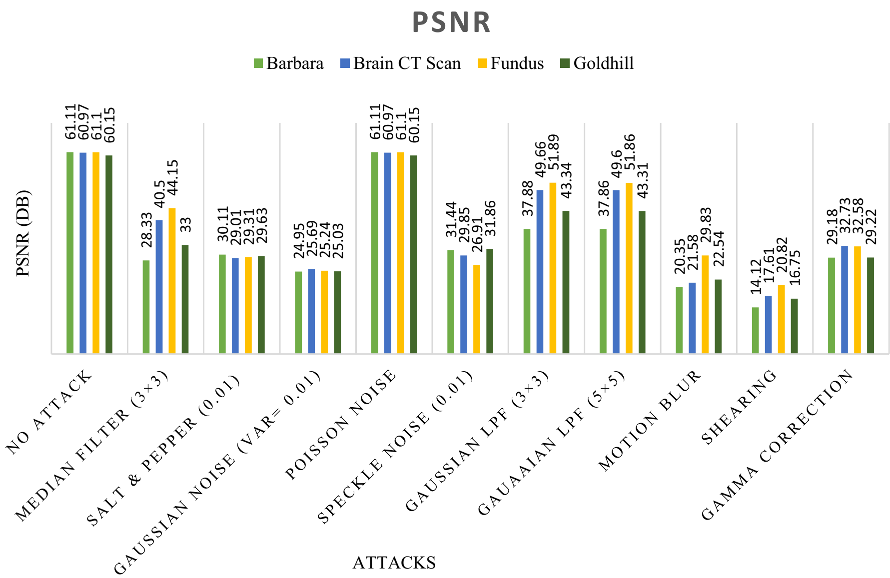

Fig. 4 PSNR of Barbara, Brain CT Scan, Fundus and Goldhill images subjected to different attacks

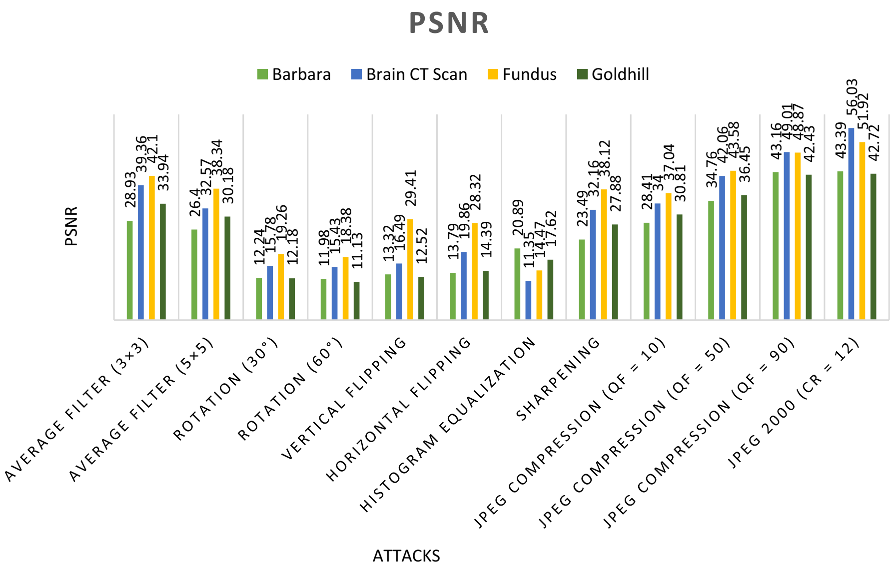

Fig. 5 PSNR values under various attacks for Barbara, Brain CT Scan, Fundus and Goldhill images

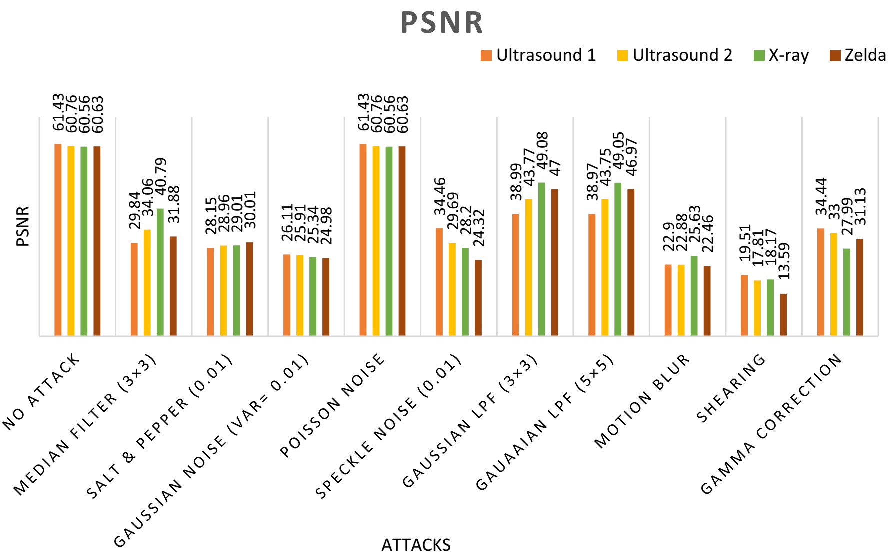

Fig. 6 Values of PSNR for different cover images under various attacks

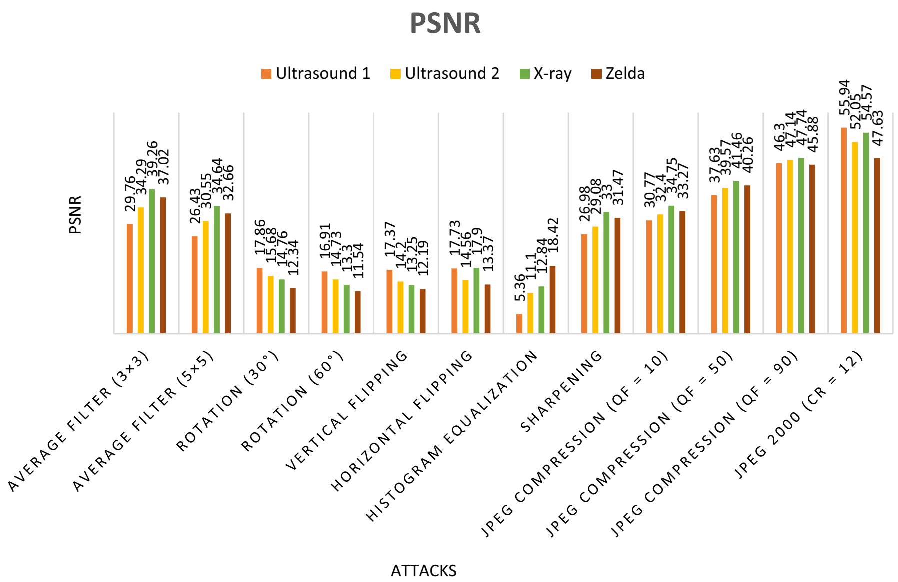

Fig. 7 Ultrasound, X-ray and Zelda cover image's PSNR values

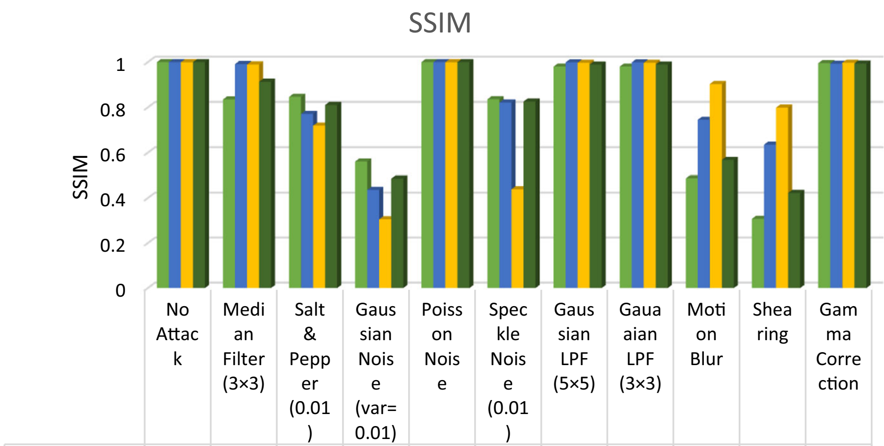

	No Attack	Median Filter (3×3)	Salt & Pepper (0.01)	Gaussian Noise (var= 0.01)	Poisson Noise	Speckle Noise (0.01)	Gaussian LPF (5×5)	Gauaaian LPF (3×3)	Motion Blur	Shearing	Gamma Correction
Barbara	0.9999	0.835	0.8465	0.5608	0.9999	0.8359	0.9802	0.9803	0.4873	0.3077	0.9953
Brain CT Scan	0.9999	0.9915	0.771	0.4359	0.9999	0.8215	0.9989	0.9989	0.7454	0.6352	0.993
Fundus	0.9995	0.9896	0.7191	0.3059	0.9995	0.4388	0.9971	0.9971	0.9035	0.7989	0.9973
Goldhill	0.9998	0.9131	0.8105	0.4861	0.9998	0.8258	0.9895	0.9894	0.5678	0.4225	0.9937

Fig. 8 SSIM of Barbara, Brain CT Scan, Fundus and Goldhill images subjected to different attacks

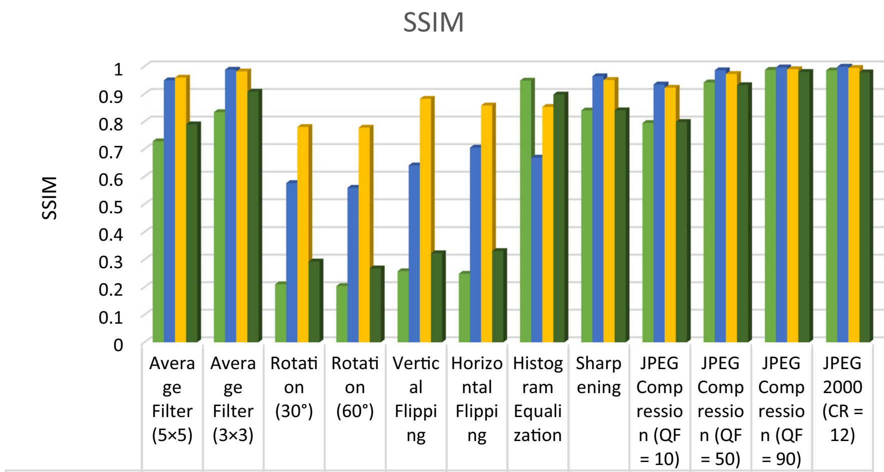

	Average Filter (5×5)	Average Filter (3×3)	Rotation (30°)	Rotation (60°)	Vertical Flipping	Horizontal Flipping	Histogram Equalization	Sharpening	JPEG Compression (QF = 10)	JPEG Compression (QF = 50)	JPEG Compression (QF = 90)	JPEG 2000 (CR = 12)
Barbara	0.7284	0.8343	0.2105	0.2043	0.258	0.2485	0.9484	0.8403	0.7947	0.942	0.9876	0.9856
Brain CT Scan	0.9497	0.988	0.577	0.5599	0.641	0.7054	0.6693	0.9644	0.9347	0.9861	0.9967	0.9991
Fundus	0.9594	0.9819	0.7803	0.7778	0.8826	0.8583	0.8533	0.9509	0.9229	0.9727	0.9901	0.9945
Goldhill	0.7901	0.9084	0.2931	0.2681	0.3232	0.3311	0.8983	0.8408	0.7987	0.932	0.98	0.9785

Fig. 9 SSIM values under various attacks for Barbara, Brain CT Scan, Fundus and Goldhill images

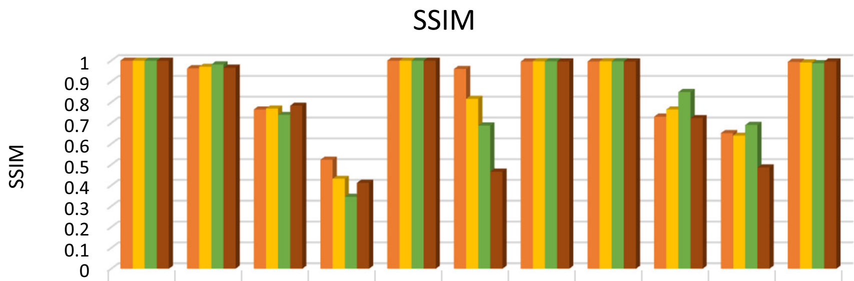

	No Attack	Median Filter (3×3)	Salt & Pepper (0.01)	Gaussian Noise (var= 0.01)	Poisson Noise	Speckle Noise (0.01)	Gaussian LPF (5×5)	Gauaai an LPF (3×3)	Motion Blur	Shearing	Gamma Correction
Ultrasound 1	0.9999	0.9633	0.7651	0.5237	0.9999	0.9598	0.9955	0.9955	0.7308	0.6515	0.9938
Ultrasound 2	0.9998	0.9703	0.7692	0.4321	0.9998	0.8163	0.9969	0.9969	0.765	0.6393	0.9913
X-ray	0.9998	0.9815	0.739	0.3455	0.9998	0.6879	0.9965	0.9966	0.849	0.6904	0.9873
Zelda	0.9998	0.9662	0.7833	0.4123	0.9998	0.4663	0.9961	0.9961	0.7238	0.486	0.9961

Fig. 10 Values of SSIM for different cover images under various attacks

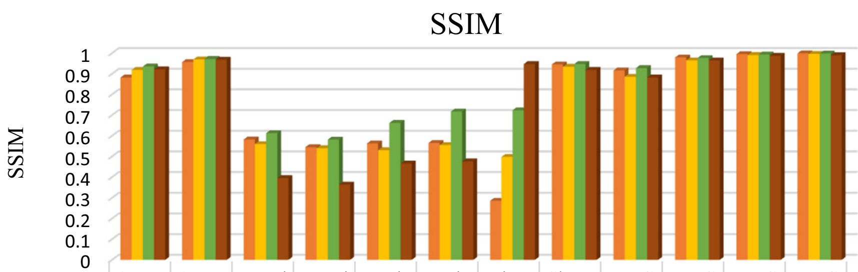

	Average Filter (5×5)	Average Filter (3×3)	Rotation (30°)	Rotation (60°)	Vertical Flipping	Horizontal Flipping	Histogram Equalization	Sharpening	JPEG Compression (QF = 10)	JPEG Compression (QF = 50)	JPEG Compression (QF = 90)	JPEG 2000 (CR = 12)
Ultrasound 1	0.8822	0.9565	0.5823	0.5445	0.5627	0.5654	0.2856	0.9451	0.9161	0.9787	0.9955	0.9993
Ultrasound 2	0.9185	0.9691	0.5594	0.5396	0.5301	0.5544	0.4977	0.934	0.8856	0.9647	0.991	0.9962
X-ray	0.9355	0.9719	0.6126	0.5814	0.6619	0.7175	0.7236	0.9471	0.9275	0.9761	0.9934	0.9983
Zelda	0.9217	0.9683	0.3951	0.3638	0.4657	0.476	0.9469	0.9187	0.8819	0.9643	0.987	0.99

Fig. 11 Ultrasound, X-ray and Zelda cover image's SSIM values

lowest value is 24.32 dB of Zelda image under speckle noise. Under several attacks, SSIM values for all cover images are shown in Figs. 8, 9, 10, 11. Performance of proposed scheme attains SSIM value above 0.85 under most of attacks except few attacks. In case of filter attacks, SSIM value 0.9989 is highest for Brain CT Scan image under Gaussian low-pass filter and SSIM value 0.7284 for Barbara image under average filter. Considering various attacks, KL DIV and JS DIV are calculated for Barbara, Brain CT Scan, Fundus and Goldhill cover images which are tabulated in Table 4.

Table 4 KL DIV and JS DIV calculated value for Barbara, Brain CT Scan, Fundus and Goldhill cover images under several attacks

Images/attacks	Barbara		Brain CT scan		Fundus		Goldhill	
	KL DIV ($\times 10^{-3}$)	JS DIV ($\times 10^{-3}$)	KL DIV ($\times 10^{-3}$)	JS DIV ($\times 10^{-3}$)	KL DIV ($\times 10^{-3}$)	JS DIV ($\times 10^{-3}$)	KL DIV ($\times 10^{-3}$)	JS DIV ($\times 10^{-3}$)
No attack	2.57×10^{-3}	6.42×10^{-4}	3.62×10^{-3}	3.62×10^{-3}	5.27×10^{-3}	1.32×10^{-3}	3.62×10^{-3}	9.06×10^{-4}
Median filter (3×3)	3.7	0.92	1.6	1.6	0.22	5.21×10^{-2}	1.6	0.40
Salt and pepper (0.01)	2.5	0.63	3.0	3.0	4.1	1.1	3.0	0.77
Gaussian noise (var = 0.01)	10.3	2.5	12.3	12.3	14.2	3.6	12.3	3.0
Poisson noise	2.57×10^{-3}	6.42×10^{-4}	3.62×10^{-3}	3.62×10^{-3}	5.27×10^{-3}	1.32×10^{-3}	3.62×10^{-3}	9.06×10^{-4}
Speckle noise (var = 0.01)	1.6	0.4	1.6	1.6	7.4	1.8	1.6	0.40
Gaussian LPF (5×5)	0.44	0.11	0.15	0.15	4.02×10^{-2}	1.01×10^{-2}	0.15	3.95×10^{-2}
Gaussian LPF (3×3)	0.44	0.11	0.15	0.15	4.00×10^{-2}	1.00×10^{-2}	0.15	3.92×10^{-2}
Average filter (5×5)	6.3	1.6	3.2	3.2	0.89	0.22	3.2	0.80
Average filter (3×3)	3.4	0.86	1.4	1.4	0.36	9.08×10^{-2}	1.4	0.34
Rotation (30°)	260.5	54.7	288.6	288.6	96.1	20.3	288.6	57.1
Rotation (60°)	264.8	56.8	350.9	350.9	105.0	22.6	350.9	71.9
Vertical flipping	135.3	32.7	158.3	158.3	5.2	1.3	158.3	38.3
Horizontal flipping	122.7	29.7	136.2	136.2	7.6	1.8	136.2	32.7
Histogram equalization	4.8	1.2	7.9	7.9	4.7	1.2	7.9	1.9
Sharpening	14.1	3.3	6.0	6.0	0.64	0.16	6.0	1.4
JPEG compression (QF = 10)	4.2	1.0	3.0	3.0	0.97	0.24	3.0	0.74
JPEG compression (QF = 50)	0.98	0.24	0.82	0.82	0.24	6.21×10^{-2}	0.82	0.20

Table 4 (continued)

Images/attacks	Barbara		Brain CT scan		Fundus		Goldhill	
	KL DIV ($\times 10^{-3}$)	JS DIV ($\times 10^{-3}$)	KL DIV ($\times 10^{-3}$)	JS DIV ($\times 10^{-3}$)	KL DIV ($\times 10^{-3}$)	JS DIV ($\times 10^{-3}$)	KL DIV ($\times 10^{-3}$)	JS DIV ($\times 10^{-3}$)
JPEG compression (QF = 90)	0.14	3.66×10^{-2}	0.21	0.21	7.59×10^{-2}	1.91×10^{-2}	0.21	5.35×10^{-2}
JPEG 2000 (CR = 12)	0.14	3.50×10^{-2}	0.2	0.20	3.13×10^{-2}	7.85×10^{-3}	0.20	5.16×10^{-2}
Motion blur (45, 45)	27.9	7.1	17.4	17.4	6.9	1.8	17.4	4.3
Shearing	185.5	37.4	114.8	114.8	78.5	15.1	114.8	23.2
Gamma correction	0.39	9.98×10^{-2}	0.59	0.59	8.99×10^{-2}	2.24×10^{-2}	0.59	0.14

Smaller the value of KL DIV and JS DIV, better is the imperceptibility of scheme. For cover images Ultrasound 1, Ultrasound 2, X-ray and Zelda, KL DIV and JS DIV are presented in Table 5. It is clear from the values of KL DIV and JS DIV calculated under several attacks which are very small, and it infers that proposed scheme performs well in terms of imperceptibility.

NC values are calculated for both the extracted watermarks, while BER is calculated only for text image watermark and expressed in percentage. NC and BER for all cover images are calculated and presented in Tables 6 and 7. For noise attacks, highest NC value is 0.9999 under Poisson noise for most of the images and lowest NC value is 0.9990 for Zelda test image under speckle noise with variance = 0.01. Lowest BER value 0.59% is achieved for Goldhill image under speckle noise. In case of filtering operations, lowest NC value is 0.9963 for Ultrasound 1 image under average filter (5 × 5) operation and highest NC value of 0.9999 is achieved for first watermark under median and Gaussian LPF for most of the test images. Lowest BER value of 0.72% is obtained for Fundus image under Gaussian LPF (3 × 3) operation.

When test images are subjected to geometric attacks, minimum NC value of 0.9983 is obtained for Ultrasound 1 image under rotation (60°) attack and maximum NC value of 0.9999 is achieved under flipping attacks for most of the test images. BER value of 0.60% is lowest for X-ray image under shearing attack. In case of image processing operations, lowest NC value of 0.9957 for ultrasound 1 image under motion blur (45, 45) operation is attained. Highest NC value of 0.9999 is achieved under JPEG compression operation for most of the images. Lowest BER value of 0.34% is attained for Fundus image under histogram equalization operation.

It is clear from Tables 6 and 7 that NC values under different attacks for all cover images are above 0.99, which shows the proposed scheme performs satisfactory in terms of robustness. BER for most of the test images under various attacks is below

Table 5 KL DIV and JS DIV calculated value for Ultrasound, X-ray and Zelda cover images under several attacks

Images/attacks	Ultrasound 1		Ultrasound 2		X-ray		Zelda	
	KL DIV ($\times 10^{-3}$)	JS DIV ($\times 10^{-3}$)	KL DIV ($\times 10^{-3}$)	JS DIV ($\times 10^{-3}$)	KL DIV ($\times 10^{-3}$)	JS DIV ($\times 10^{-3}$)	KL DIV ($\times 10^{-3}$)	JS DIV ($\times 10^{-3}$)
No attack	1.69×10^{-2}	4.22×10^{-3}	1.03×10^{-2}	2.57×10^{-3}	4.21×10^{-3}	1.05×10^{-3}	3.39×10^{-3}	8.48×10^{-4}
Median filter (3×3)	13.3	3.1	4.1	0.94	0.30	7.69×10^{-2}	1.6	0.38
Salt and pepper (0.01)	19.7	6.0	8.2	2.4	5.8	1.6	2.8	0.72
Gaussian noise (var = 0.01)	54.8	14.0	29.0	7.3	24.8	6.0	10.6	2.6
Poisson noise	1.69×10^{-2}	4.22×10^{-3}	1.03×10^{-2}	2.57×10^{-3}	4.21×10^{-3}	1.05×10^{-3}	3.39×10^{-3}	8.48×10^{-4}
Speckle noise (var = 0.01)	4.2	1.1	6.1	1.5	6.8	1.7	8.8	2.2
Gaussian LPF (5×5)	2.1	0.54	0.45	0.11	5.79×10^{-2}	1.44×10^{-2}	8.22×10^{-2}	2.09×10^{-2}
Gaussian LPF (3×3)	2.1	0.53	0.44	0.11	5.75×10^{-2}	1.43×10^{-2}	8.16×10^{-2}	2.08×10^{-2}
Average filter (5×5)	35.9	9.0	7.6	1.9	1.6	0.38	1.9	0.49
Average filter (3×3)	15.5	4.0	3.5	0.89	0.57	0.14	0.74	0.19
Rotation (30°)	331.0	75.3	237.9	53.5	207.3	49.0	263.2	55.4
Rotation (60°)	425.1	97.5	291.0	66.6	276.7	65.9	297.4	64.2
Vertical flipping	359.4	81.1	303.8	70.5	247.7	58.2	191.4	45.5
Horizontal flipping	350.2	79.0	284.8	65.5	88.2	21.2	146.1	34.8
Histogram equalization	197.5	45.0	39.0	9.6	35.5	8.5	2.9	0.70
Sharpening	20.3	4.9	7.8	1.9	2.3	0.56	2.2	0.52
JPEG Compression (QF = 10)	16.1	4.1	6.8	1.7	2.0	0.48	1.7	0.42
JPEG Compression (QF = 50)	4.0	1.0	1.5	0.36	0.34	8.71×10^{-2}	0.32	8.15×10^{-2}

Table 5 (continued)

Images/attacks	Ultrasound 1		Ultrasound 2		X-ray		Zelda	
	KL DIV ($\times 10^{-3}$)	JS DIV ($\times 10^{-3}$)	KL DIV ($\times 10^{-3}$)	JS DIV ($\times 10^{-3}$)	KL DIV ($\times 10^{-3}$)	JS DIV ($\times 10^{-3}$)	KL DIV ($\times 10^{-3}$)	JS DIV ($\times 10^{-3}$)
JPEG Compression (QF = 90)	0.66	0.16	0.28	7.13×10^{-2}	8.05×10^{-2}	2.01×10^{-2}	8.90×10^{-2}	2.23×10^{-2}
JPEG 2000 (CR = 12)	7.59×10^{-2}	1.90×10^{-2}	9.58×10^{-2}	2.39×10^{-2}	2.24×10^{-2}	5.62×10^{-3}	5.69×10^{-2}	1.42×10^{-2}
Motion blur (45, 45)	98.2	22.3	40.4	9.7	13.4	3.3	19.4	5.0
Shearing	230.8	51.4	149.9	33.1	106.1	24.6	228.6	43.5
Gamma correction	1.8	0.45	0.66	0.16	0.75	0.18	0.376	9.44×10^{-2}

1.5% which shows the proposed scheme withstand attacks without degrading the quality of extracted text image watermark.

5.3 Embedding Capacity Analysis

Main advantage of RDWT is that the size after decomposing the image at various levels does not change. After three-level RDWT, the size of the third-level sub-band for the 512 $\times$ 512 host image remains the same, and the third-level sub-band of the host image is used for watermark embedding. Watermark image size remains same as 512 $\times$ 512 after applying 1-level RDWT in the embedding procedure. The ratio of total number of pixels of watermark to the total number of cover image's pixel is defined as the capacity of watermarking scheme.

Thus, the capacity of proposed scheme is $\frac{512\times512}{512\times512} = 1$, which shows the technique has high capacity. Embedding capacity comparison of proposed scheme with related works is presented in Table 14.

5.4 Computational Complexity Analysis

Computational complexity is analyzed in terms of execution time and is expressed in seconds. Embedding time including encryption in proposed schemes takes 1.3985 s, while extraction time including decryption takes 0.6653 s. Thus, total execution time for proposed scheme is 2.0638 s. Comparison of computational complexity of proposed scheme with existing works is listed in Table 15. It is clear from comparison that proposed scheme is computationally efficient.

Performance of proposed technique is also assessed by optimizing the strength factor using particle swarm optimization (PSO) technique [19], and parameter values

Table 6 NC and BER values for Barbara, Brain CT Scan, Fundus and Goldhill cover images under several attacks

Images/attacks	Barbara			Brain CT scan			Fundus			Goldhill		
	NC1	NC2	BER (%)	NC1	NC2	BER (%)	NC1	NC2	BER (%)	NC1	NC2	BER (%)
No attack	0.9999	0.9998	0.60	0.9999	0.9998	0.60	0.9999	0.9998	0.61	0.9999	0.9998	0.59
Median filter (3 × 3)	0.9998	0.9986	1.91	0.9999	0.9995	1.03	0.9999	0.9997	0.80	0.9998	0.9994	1.19
Salt and pepper (0.01)	0.9998	0.9998	0.65	0.9996	0.9998	0.90	0.9996	0.9998	0.77	0.9998	0.9998	0.65
Gaussian noise (var = 0.01)	0.9994	0.9998	0.95	0.9993	0.9997	1.14	0.9991	0.9996	1.18	0.9995	0.9997	0.99
Poisson noise	0.9999	0.9998	0.60	0.9999	0.9998	0.60	0.9999	0.9998	0.61	0.9999	0.9998	0.59
Speckle noise (var = 0.01)	0.9998	0.9998	0.62	0.9997	0.9998	0.67	0.9993	0.9997	0.98	0.9998	0.9999	0.59
Gaussian LPF (5 × 5)	0.9999	0.9994	1.15	0.9999	0.9997	0.78	0.9999	0.9997	0.72	0.9999	0.9996	0.86
Gaussian LPF (3 × 3)	0.9999	0.9994	1.15	0.9999	0.9997	0.78	0.9999	0.9997	0.72	0.9999	0.9997	0.86
Average filter (5 × 5)	0.9995	0.9964	3.11	0.9998	0.9989	1.60	0.9999	0.9994	1.15	0.9996	0.9985	1.90
Average filter (3 × 3)	0.9998	0.9982	2.16	0.9999	0.9994	1.14	0.9999	0.9996	0.93	0.9998	0.9992	1.38
Rotation (30°)	0.9998	0.9993	1.43	0.9999	0.9996	0.86	0.9998	0.9997	0.87	0.9998	0.9997	0.82
Rotation (60°)	0.9998	0.9989	1.75	0.9998	0.9995	1.04	0.9998	0.9997	0.79	0.9999	0.9997	0.90
Vertical flipping	0.9999	0.9998	0.60	0.9999	0.9998	0.60	0.9999	0.9998	0.61	0.9999	0.9998	0.59
Horizontal flipping	0.9999	0.9998	0.60	0.9999	0.9998	0.60	0.9999	0.9998	0.61	0.9999	0.9998	0.59
Histogram equalization	0.9997	0.9999	0.65	0.9999	0.9997	0.81	0.9998	1.0000	0.34	0.9996	1.0000	0.36
Sharpening	0.9989	0.9968	3.04	0.9996	0.9998	0.69	0.9998	1.0000	0.39	0.9988	0.9993	1.36
JPEG Compression (QF = 10)	0.9999	0.9996	1.00	0.9999	0.9998	0.64	0.9999	0.9997	0.79	0.9999	0.9997	0.87
JPEG compression (QF = 50)	0.9999	0.9998	0.64	0.9999	0.9998	0.63	0.9999	0.9998	0.70	0.9999	0.9998	0.64
JPEG compression (QF = 90)	0.9999	0.9998	0.61	0.9999	0.9998	0.61	0.9999	0.9998	0.64	0.9999	0.9998	0.60

Table 6 (continued)

Images/attacks	Barbara			Brain CT scan			Fundus			Goldhill		
	NC1	NC2	BER (%)	NC1	NC2	BER (%)	NC1	NC2	BER (%)	NC1	NC2	BER (%)
JPEG 2000 (CR = 12)	0.9999	0.9998	0.62	0.9999	0.9998	0.61	0.9999	0.9998	0.63	0.9999	0.9998	0.62
Motion blur (45, 45)	0.9994	0.9959	3.29	0.9997	0.9986	1.80	0.9999	0.9993	1.24	0.9995	0.9983	2.05
Shearing	0.9999	0.9997	0.96	0.9999	0.9998	0.64	0.9999	0.9998	0.68	0.9999	0.9997	0.79
Gamma correction	0.9999	0.9998	0.63	0.9999	0.9998	0.64	0.9999	0.9998	0.56	0.9999	0.9998	0.58

Table 7 NC and BER values for Pepper, Sailboat and Ultrasound 1 cover images under several attacks

Images/attacks	Ultrasound 1			Ultrasound 2			X-ray			Zelda		
	NC1	NC2	BER (%)	NC1	NC2	BER (%)	NC1	NC2	BER (%)	NC1	NC2	BER (%)
No attack	0.9999	0.9998	0.61	0.9999	0.9998	0.60	0.9999	0.9998	0.60	0.9999	0.9998	0.60
Median filter (3 × 3)	0.9998	0.9986	1.75	0.9999	0.9993	1.34	0.9999	0.9996	0.95	0.9999	0.9995	1.09
Salt and pepper (0.01)	0.9997	0.9998	0.82	0.9996	0.9998	0.85	0.9996	0.9998	0.82	0.9997	0.9998	0.76
Gaussian noise (var = 0.01)	0.9997	0.9997	0.92	0.9993	0.9997	1.14	0.9993	0.9997	1.14	0.9992	0.9996	1.25
Poisson noise	0.9999	0.9998	0.61	0.9999	0.9998	0.60	0.9999	0.9998	0.60	0.9999	0.9998	0.60
Speckle noise (var = 0.01)	0.9999	0.9998	0.61	0.9997	0.9998	0.76	0.9996	0.9999	0.61	0.9990	0.9995	1.32
Gaussian LPF (5 × 5)	0.9999	0.9994	1.16	0.9999	0.9996	0.94	0.9999	0.9997	0.76	0.9999	0.9997	0.81
Gaussian LPF (3 × 3)	0.9999	0.9994	1.15	0.9999	0.9996	0.93	0.9999	0.9997	0.76	0.9999	0.9997	0.81
Average filter (5 × 5)	0.9992	0.9963	3.01	0.9997	0.9980	2.24	0.9998	0.9992	1.40	0.9997	0.9988	1.69
Average filter (3 × 3)	0.9996	0.9979	2.20	0.9998	0.9990	1.60	0.9999	0.9995	1.06	0.9998	0.9993	1.23
Rotation (30°)	0.9998	0.9987	1.72	0.9998	0.9991	1.48	0.9998	0.9997	0.75	0.9998	0.9996	1.00
Rotation (60°)	0.9998	0.9983	1.96	0.9997	0.9988	1.76	0.9998	0.9997	0.78	0.9997	0.9995	1.13
Vertical flipping	0.9999	0.9998	0.61	0.9999	0.9998	0.60	0.9999	0.9998	0.60	0.9999	0.9998	0.60
Horizontal flipping	0.9999	0.9998	0.61	0.9999	0.9998	0.60	0.9999	0.9998	0.60	0.9999	0.9998	0.60
Histogram equalization	0.9998	0.9988	1.65	0.9991	0.9996	1.17	0.9999	0.9998	0.65	0.9998	1.0000	0.35
Sharpening	0.9990	0.9994	1.25	0.9995	0.9994	1.35	0.9996	0.9998	0.68	0.9996	0.9997	0.93
JPEG compression (QF = 10)	0.9999	0.9996	0.93	0.9999	0.9997	0.79	0.9999	0.9997	0.76	0.9999	0.9998	0.74
JPEG compression (QF = 50)	0.9999	0.9997	0.71	0.9999	0.9998	0.66	0.9999	0.9998	0.64	0.9999	0.9998	0.67
JPEG compression (QF = 90)	0.9999	0.9998	0.63	0.9999	0.9998	0.61	0.9999	0.9998	0.60	0.9999	0.9998	0.62
JPEG 2000 (CR = 12)	0.9999	0.9998	0.61	0.9999	0.9998	0.62	0.9999	0.9998	0.60	0.9999	0.9998	0.62

Table 7 (continued)

Images/attacks	Ultrasound 1			Ultrasound 2			X-ray			Zelda		
	NC1	NC2	BER (%)	NC1	NC2	BER (%)	NC1	NC2	BER (%)	NC1	NC2	BER (%)
Motion blur (45, 45)	0.9990	0.9957	3.27	0.9996	0.9978	2.43	0.9998	0.9990	1.50	0.9997	0.9986	1.83
Shearing	0.9999	0.9992	1.27	0.9999	0.9997	0.83	0.9999	0.9998	0.60	0.9999	0.9997	0.80
Gamma correction	0.9999	0.9999	0.45	0.9999	0.9998	0.59	0.9999	0.9998	0.58	0.9999	0.9998	0.61

Table 8 Performance of proposed technique for different images under no attacks by utilizing PSO technique

Images	PSNR	SSIM	NC1	NC2	BER	KLDIS ($\times 10^{-6}$)	JSDIS ($\times 10^{-6}$)
Airplane	58.64	0.9997	0.9999	0.9998	0.60	1.94	0.486
Barbara	59.17	0.9998	0.9999	0.9998	0.60	4.01	1.00
Brain CT Scan	60.36	0.9998	0.9999	0.9998	0.62	11	2.81
Fundus	59.18	0.9993	0.9999	0.9998	0.61	8.11	2.03
Goldhill	58.21	0.9997	0.9999	0.9998	0.59	5.67	1.41
Mandrill	58.21	0.9999	0.9999	0.9998	0.59	3.52	0.88
Peppers	58.77	0.9997	0.9999	0.9998	0.60	4.02	1.00
Sailboat	58.58	0.9998	0.9999	0.9998	0.60	3.86	0.96
Ultrasound 1	59.53	0.9999	0.9999	0.9998	0.61	25	6.44
Ultrasound 2	58.84	0.9997	0.9999	0.9998	0.60	16	3.99
X-ray	58.62	0.9996	0.9999	0.9998	0.60	6.58	1.64
Zelda	58.70	0.9997	0.9999	0.9998	0.60	5.24	1.31
Average of 100 images [37]	58.56	0.9997	0.9999	0.9998	0.60	4.82	1.45

for different cover images under no attacks are listed in Table 8. Strength factor is calculated by using objective function expressed in Eq. (44). Maximum PSNR value of 60.36 dB is obtained for Brain CT Scan image, and minimum value of 58.21 dB is attained for Goldhill image. Highest SSIM is 0.9999 for Mandrill and Ultrasound 1 image. NC value is 0.9999 for first watermark, while in case of second watermark, NC is 0.9998. Graphical comparison of PSNR values obtained using MRFO and PSO technique is shown in Fig. 12. It is clear from Fig. 12 that MRFO technique provides better PSNR values in comparison with PSO for different images.

5.5 Security Analysis

Henon map is used to enhance the security of proposed technique. Henon attractor is referred as the collection of all points for which the iterations of each point in a particular quadrilateral encircle the Henon attractor. Given that its formulas mentioned in Eq. (6) have a maximum power of 2, it is an illustration of a quadratic strange attractor. The nonlinearity and dissipation are controlled by the parameters 'a' and 'b'. Henon attractor is shown in Fig. 13 for control parameter values $a = 1.4$ and $b = 0.34$. Security analysis of proposed scheme is evaluated in terms of Lyapunov exponent (LE) [9] and correlation coefficient (CC). The LE and CC is a well-known metric for quantifying the chaotic behavior of dynamical systems. The LE calculates how much two closely spaced trajectories diverge from one another. A positive LE denotes a system's excessive sensitivity to initial conditions and chaotic motion, whereas a negative LE denotes a system's stability and non-chaotic motion. Mathematically, LE

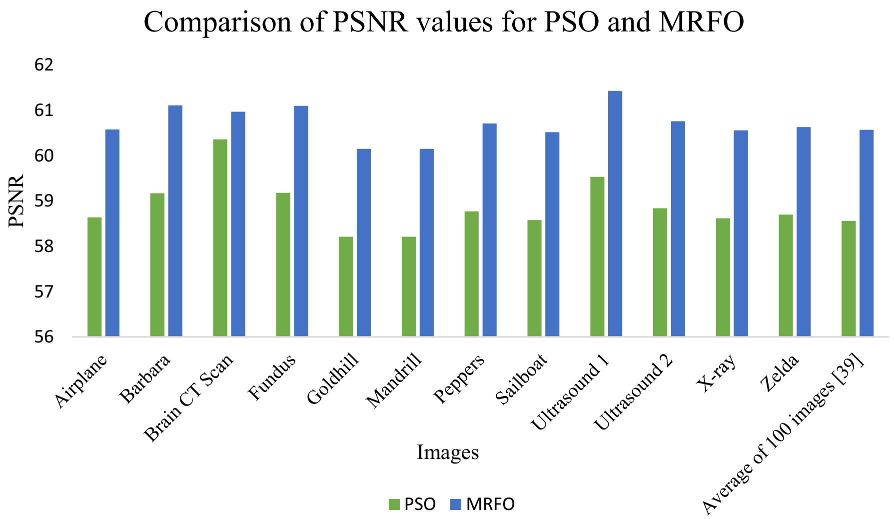

Fig. 12 Comparison of PSNR values for different images using PSO and MRFO

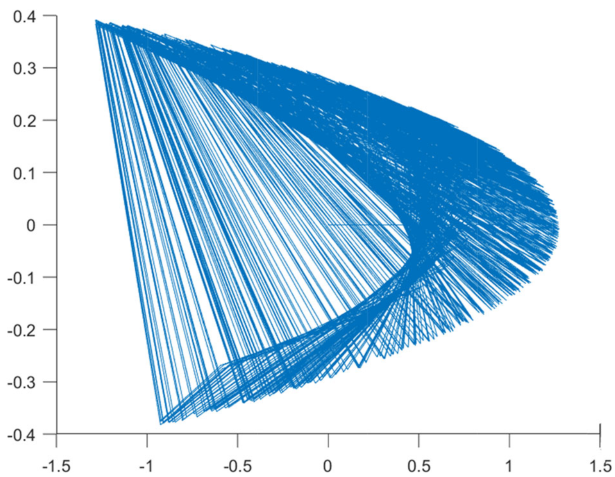

Fig. 13 Henon attractor for control parameter value $a = 1.4$, $b = 0.34$

is expressed as Eq. (57):

$$LE = \lim_{p \to \infty} \frac{1}{p} \sum_{i=1}^{p-1} \ln|f(x_i)| \tag{57}$$

where f is Henon map. The LE values of Henon map for different images with $a = 1$, $b = 1$ and $a = 1.4$, $b = 0.34$ are listed in Table 9. Maximum LE is obtained for Ultrasound 2 with LE1 = 8.92, LE2 = 12.63.

Table 9 LE values for different images using Henon map encryption

Images	$a = 1, b = 1$ LE1	$a = 1.4, b = 0.34$ LE2
Airplane	2.30	2.48
Barbara	5.00	3.57
Brain CT scan	5.09	6.45
Fundus	3.80	0.45
Goldhill	4.93	6.65
Mandrill	2.47	1.69
Peppers	3.88	3.48
Sailboat	4.33	4.67
Ultrasound 1	7.23	6.56
Ultrasound 2	8.92	12.63
X-ray	6.48	8.18
Zelda	7.57	8.04

The CC measures the distance between two chaotic sequences that are produced from the chaotic map under slightly varied initial conditions and system characteristics. It is expressed as Eq. (58):

$$CC(P, Q) = \frac{E\left[(P - \mu_P)\left(Q - \mu_Q\right)\right]}{\sigma_P \sigma_Q} \tag{58}$$

μ_P and μ_Q are the mean of chaotic sequences P and Q, σ_P and σ_Q are the standard deviation of P and Q, respectively. Two chaotic sequences are said to be close to one another, if CC values are close to '1' and sequences are entirely different, if CC values are close to '0'. CC values for different images with $a = 1$, $b = 1$ and $a = 1.4$, $b = 0.34$ are listed in Table 10. It is evident from Table 10 that CC values are very close to '0' for parameter values $a = 1.4$, $b = 0.34$. Thus, the proposed technique provides enhanced security for $a = 1.4$, $b = 0.34$.

6 Comparison with Existing Techniques

Performance of suggested method is compared with some recent state-of-the-art watermarking techniques presented in [15, 18, 23–25, 28, 31, 38–40]. Table 11 presents the PSNR, SSIM and NC comparison for Airplane, Mandrill, Pepper and Sailboat images without attacks. Comparison is shown for those images which are common in all techniques. It is clear from Table 11 that proposed method performs better in terms of imperceptibility. Average percentage improvement is 13.76% for PSNR when compared with existing mentioned techniques. For NC without attacks, average percentage improvement is 4.3% in case of non-medical images. Under no attacks, PSNR and SSIM values comparison of medical image is listed in Table 12. For medical image,

Table 10 CC values of Henon map with varying parameter values of a and b for different images

Images	$a = 1, b = 1$	$a = 1.4, b = 0.34$
Airplane	0.0142	1.26×10^{-5}
Barbara	0.0626	0.0343
Brain CT Scan	0.1295	− 0.0134
Fundus	0.1803	0.0184
Goldhill	0.0146	− 0.1157
Mandrill	0.0111	0.0063
Peppers	0.0145	− 0.0546
Sailboat	0.1106	0.0279
Ultrasound 1	0.0043	− 0.0315
Ultrasound 2	0.1453	3.63×10^{-4}
X-ray	0.0195	0.0053
Zelda	0.0492	0.0071

Table 11 Comparison of PSNR, SSIM and NC values of proposed scheme with some existing techniques for non-medical images

Parameter	Scheme	Host image			
		Airplane	Mandrill	Pepper	Sailboat
PSNR	[23]	–	54.35	53.89	–
	[31]	56.44	57.37	57.60	–
	[18]	52.11	52.12	52.18	52.09
	[39]	–	51.42	50.62	50.73
	Proposed	60.58	60.15	60.71	60.52
	Average percentage Improvement	11.78	11.98	13.57	17.73
SSIM	[23]	–	0.9999	0.9999	–
	[31]	0.9986	0.9901	0.9991	–
	[18]	0.9971	0.9997	0.9998	0.9995
	[39]	–	–	–	–
	Proposed	0.9998	0.9999	0.9998	0.9999
NC	[23]	–	1.0000	1.0000	–
	[31]	0.9457	0.6943	0.9577	–
	[18]	1.0000	1.0000	1.0000	0.9705
	[39]	–	0.9979	0.9871	0.9918
	Proposed	0.9999	0.9998	0.9999	0.9999
	Average percentage Improvement	2.86	11.03	1.41	1.91

Table 12 Comparison of imperceptibility analysis for medical image with related works

[15]		[28]		[24]		[23]		[25]		Proposed	
PSNR	SSIM	PSNR	SSIM	PSNR	SSIM	PSNR	SSIM	PSNR	SSIM	PSNR	SSIM
55.85	0.9997	48.53	–	36.10	0.9961	37.57	0.9812	43.30	0.9923	60.97	0.9999

Table 13 Robustness comparison of proposed scheme with state-of-the-art schemes for medical image in terms of NC

Attacks/scheme	[15]	[28]	[24]	[23]	[25]	Proposed
No attack	–	0.9932	0.9835	0.9998	0.9985	0.9999
Gaussian LPF	0.9584	–	–	–	–	0.9999
Gaussian noise (var = 0.01)	0.9118	0.9985	–	0.9984	0.9655	0.9993
Average filter (3 × 3)	0.9731	–	–	–	–	0.9999
Histogram equalization	0.8455	0.9835	0.7223	0.9990	0.565	0.9999
Salt and pepper (0.01)	–	0.8416	–	0.9996	–	0.9996
Speckle noise (var = 0.01)	0.9818	–	–	0.9988	–	0.9997
Median filter (3 × 3)	0.9093	–	–	0.9989	0.7341	0.9999
JPEG compression (QF = 50)	–	–	0.9388	–	0.9825	0.9999
Sharpening	0.8119	–	0.6381	–	0.8716	0.9996
Rotation (30°)	0.8564	–	–	–	–	0.9999
Gamma correction	–	0.9856	–	–	–	0.9999

average percentage improvement is 41.35% in terms of PSNR. Robustness comparison of proposed method with other methods for medical and non-medical images is tabulated in Tables 13 and 16, respectively. NC value comparison is shown for those attacks only which are common in existing methods. Dash is shown for those attacks or cover images where analysis is not reported. From Tables 13 and 16, it is clear that obtained NC values are 0.99 for proposed technique when subjected to various attacks. Average percentage improvement is 0.62% for medical image in terms of NC when no attack is applied. From robustness comparison, it is depicted that proposed method performs better when subjected to various attacks.

Embedding capacity of proposed technique is compared with embedding capacity of state-of-the-art techniques and is presented in Table 14. Proposed scheme utilized RDWT and dual watermarks for embedding, and hence, embedding capacity of '1' is achieved. Existing schemes achieve capacity near about 0.25. So, it can be concluded that proposed scheme provides higher embedding capacity as compared with existing techniques.

Computational complexity of proposed scheme is listed in Table 15 along with complexity of existing schemes mentioned in [24, 25, 40]. Embedding time shown here also includes the encryption time and is expressed in seconds. Extraction time includes the decryption time and is shown in table. Scheme mentioned in [24] takes

Table 14 Comparison of embedding capacity with existing schemes

[24]	[40]	[25]	[38]	Proposed
0.25	0.25	0.25	0.25	1

Table 15 Computational complexity comparison in terms of total execution time with related techniques

Time Complexity (msec)	[24]	[40]	[25]	Proposed
Embedding + encryption	6493.4	3979.0	1569.8	1398.5
Extraction + decryption	11,918.2	2010.4	498.5	665.3
Total time	18,411.6	5989.4	2068.3	2063.8

14.8116 s for execution, while [40] takes 5.9894 s. Scheme [25] takes 2.0683 s during execution, while proposed scheme takes total 2.0638 s. It is evident from Table 15 that proposed scheme is computationally efficient as compared to existing schemes (Table 16).

7 Conclusion

In this paper, an optimized dual image watermarking based on RDWT-RSVD using MRFO technique with Henon mapping is proposed. Dual watermarks are utilized for embedding to enhance capacity and security of proposed technique. Luminance component of YCbCr color space is used for embedding. To achieve a balance among robustness, capacity and imperceptibility, an optimum strength factor is chosen by MRFO technique. Additionally, the proposed technique further enhances the security by encrypting dual watermarks before embedding using Henon map. Extensive experiments are performed on various medical and non-medical images demonstrating that proposed technique provides superiority when compared with existing schemes in terms of embedding capacity, imperceptibility and robustness. Performance of proposed technique is also evaluated by obtaining optimized strength factor using PSO. The proposed scheme is computationally efficient as compared to state-of-the-art schemes. Average PSNR value for 100 images is 60.57 dB with SSIM value of 0.9998 using MRFO, while using PSO, average PSNR value of 58.56 dB is obtained with SSIM value of 0.9997. Overall results show that MRFO performs better in comparison with PSO. In future, machine learning techniques can be applied to optimize scaling factor which can further enhance the performance of proposed watermarking scheme.

Table 16 Robustness comparison of proposed method with state-of-the-art watermarking techniques for non-medical images in terms of NC values subjected to several attacks

Attacks/images	Airplane				Mandrill				Pepper				Sailboat			
	[31]	[18]	[39]	Proposed	[31]	[18]	[39]	Proposed	[31]	[18]	[39]	Proposed	[31]	[18]	[39]	Proposed
Median filter (3 × 3)	0.9848	–	–	0.9998	0.8607	0.9665	0.9464	0.9990	0.9929	0.9848	0.9540	0.9998	–	–	0.9512	0.9996
Gaussian noise (var = 0.01)	–	–	–	0.9995	–	–	0.9284	0.9997	–	–	0.9387	0.9995	–	–	0.9295	0.9996
Speckle noise (var = 0.01)	–	–	–	0.9987	–	–	0.9593	0.9998	–	–	0.9639	0.9998	–	–	0.9658	0.9998
Gaussian LPF (3 × 3)	0.9987	–	–	0.9999	0.8947	0.9657	0.9841	0.9997	0.9997	0.9852	0.9753	0.9999	–	–	0.9845	0.9999
Average filter (3 × 3)	–	–	–	0.9998	–	0.9687	0.9738	0.9987	–	0.9865	0.9741	0.9998	–	–	0.9820	0.9997
Histogram equalization	0.9929	–	–	0.9993	0.9296	0.9455	0.9235	0.9989	0.9994	0.9717	0.9456	0.9998	–	–	0.9271	0.9999
Sharpening	0.9994	–	–	0.9986	0.9351	0.9545	0.9329	0.9934	0.9997	0.9754	0.9366	0.9992	–	–	0.9159	0.9979
JPEG compression (QF = 50)	0.6630	–	–	0.9999	0.6029	0.9688	0.9787	0.9998	0.6772	0.9863	0.9807	0.9999	–	–	0.9747	0.9999
JPEG compression (QF = 90)	0.9990	–	–	0.9999	0.9296	–	0.9963	0.9998	0.9984	–	0.9938	0.9999	–	–	0.9939	0.9999
Motion blur	0.9800	–	–	0.9992	0.7861	–	–	0.9964	0.9780	–	–	0.9995	–	–	–	0.9990
Shearing	–	–	–	0.9999	–	0.9677	0.8895	0.9998	–	0.9858	0.8817	0.9999	–	–	0.8951	0.9999

Data Availability My manuscript has no associated data.

Declarations

Conflict of Interest The authors declare that they have no conflict of interest.

References

1. R.Y. Abadi, P. Moallem, Robust and optimum color image watermarking method based on a combination of DWT and DCT. Optik **261**, 169146 (2022)
2. A. Chacko, S. Chacko, Deep learning-based robust medical image watermarking exploiting DCT and Harris hawks optimization. Int. J. Intell. Syst. **37**(8), 4810–4844 (2022)
3. S. Chauhan, M. Singh, A.K. Aggarwal, Investigative analysis of different mutation on diversity-driven multi-parent evolutionary algorithm and its application in area coverage optimization of WSN. Soft Comput. 1–27 (2023)
4. R. Dwivedi, V.K. Srivastava, An Imperceptible and Robust image watermarking using RDWT and SVD in YCbCr color space, in *IEEE 9th Uttar Pradesh Section International Conference on Electrical, Electronics and Computer Engineering (UPCON)* (IEEE, 2022), pp. 1–5
5. R. Dwivedi, V.K. Srivastava, Fundamental optimization methods for machine learning, in *Statistical Modeling in Machine Learning* (Academic Press, 2023), pp. 227–247
6. A. Fkirin, G. Attiya, A. El-Sayed, M.A. Shouman, Copyright protection of deep neural network models using digital watermarking: a comparative study. Multimedia Tools Appl. **81**(11), 15961–15975 (2022)
7. T. Konda, Y. Nakamura, A new algorithm for singular value decomposition and its parallelization. Parallel Comput. **35**(6), 331–344 (2009)
8. E. Najafi, K. Loukhaoukha, Hybrid secure and robust image watermarking scheme based on SVD and sharp frequency localized contourlet transform. J. Inf. Secur. Appl. **44**, 144–156 (2019)
9. R. Parvaz, M. Zarebnia, A combination chaotic system and application in color image encryption. Opt. Laser Technol. **101**, 30–41 (2018)
10. E. Reinhard, T. Pouli, Colour spaces for colour transfer, in *Computational Color Imaging: 3rd International Workshop, (CCIW 2011), Proceedings*, vol. 3 (pp. 1–15)
11. K. Swaraja, K. Meenakshi, P. Kora, Hierarchical multilevel framework using RDWT-QR optimized watermarking in telemedicine. Biomed. Signal Process. Control **68**, 102688 (2021)
12. F.N. Thakkar, V.K. Srivastava, A fast watermarking algorithm with enhanced security using compressive sensing and principle components and its performance analysis against a set of standard attacks. Multimedia Tools Appl **76**, 15191–15219 (2017)
13. C. Varol, C. Bayrak, Estimation of quality of service in spelling correction using Kullback–Leibler divergence. Expert Syst. Appl. **38**(5), 6307–6312 (2011)
14. A. Zear, P.K. Singh, Secure and robust color image dual watermarking based on LWT-DCT-SVD. Multimedia Tools Appl. **81**(19), 26721–26738 (2022)
15. N. Zermi, A. Khaldi, M.R. Kafi, F. Kahlessenane, S. Euschi, Robust SVD-based schemes for medical image watermarking. Microprocess. Microsyst. **84**, 104134 (2021)
16. N. Zermi, A. Khaldi, R. Kafi, F. Kahlessenane, S. Euschi, A DWT-SVD based robust digital watermarking for medical image security. Forens. Sci. Int. **320**, 110691 (2021)
17. H.T. Hu, L.Y. Hsu, T.T. Lee, All-round improvement in DCT-based blind image watermarking with visual enhancement via denoising autoencoder. Comput. Electr. Eng. **100**, 107845 (2022)
18. R. Singh, A. Ashok, M. Saraswat, High embedding capacity based color image watermarking scheme using SBBO in RDWT domain. Multimedia Tools Appl. 1–36 (2022)
19. D. Awasthi, V.K. Srivastava, LWT-DCT-SVD and DWT-DCT-SVD based watermarking schemes with their performance enhancement using Jaya and Particle swarm optimization and comparison of results under various attacks. Multimedia Tools Appl. **81**(18), 25075–25099 (2022)
20. A. Tiwari, V.K. Srivastava, A chaotic encrypted reliable image watermarking scheme based on integer wavelet transform-Schur transform and singular value decomposition, in *2022 International Conference on Computing, Communication, and Intelligent Systems (ICCCIS)* (IEEE 2022), pp. 581–586
21. J.S. Pan, X.X. Sun, S.C. Chu, A. Abraham, B. Yan, Digital watermarking with improved SMS applied for QR code. Eng. Appl. Artif. Intell. **97**, 104049 (2021)

22. M. Begum, J. Ferdush, M.S. Uddin, A Hybrid robust watermarking system based on discrete cosine transform, discrete wavelet transform, and singular value decomposition. J. King Saud Univers.-Comput. Inf. Sci. **34**(8), 5856–5867 (2022)
23. P. Sivananthamaitrey, P.R. Kumar, Optimal dual watermarking of color images with SWT and SVD through genetic algorithm. Circuits Syst. Signal Process. **41**, 224–248 (2022)
24. A. Anand, A.K. Singh, An improved DWT-SVD domain watermarking for medical information security. Comput. Commun. **152**, 72–80 (2020)
25. A. Anand, A.K. Singh, Hybrid nature-inspired optimization and encryption-based watermarking for e-healthcare. IEEE Trans. Comput. Soc. Syst. (2022)
26. R. Chellappan, S. Satheeskumaran, C. Venkatesan, S. Saravanan, Discrete stationary wavelet transform and SVD-based digital image watermarking for improved security. Int. J. Comput. Sci. Eng. **24**(4), 354–362 (2021)
27. H.S. Devi, K.M. Singh, Red-cyan anaglyph image watermarking using DWT, Hadamard transform and singular value decomposition for copyright protection. J. Inf. Secur. Appl. **50**, 102424 (2020)
28. Y. Gangadhar, V.G. Akula, P.C. Reddy, An evolutionary programming approach for securing medical images using watermarking scheme in invariant discrete wavelet transformation. Biomed. Signal Process. Control **43**, 31–40 (2018)
29. S. Han, M. Lv, Z. Cheng, Dual-color blind image watermarking algorithm using the graph-based transform in the stationary wavelet transform domain. Optik **268**, 169832 (2022)
30. D. Liu, Q. Su, Z. Yuan, X. Zhang, A fusion-domain color image watermarking based on Haar transform and image correction. Expert Syst. Appl. **170**, 114540 (2021)
31. R. Thanki, A. Kothari, S. Borra, Hybrid, blind and robust image watermarking: RDWT–NSCT based secure approach for telemedicine applications. Multimedia Tools Appl. **80**(18), 27593–27613 (2021)
32. S. Wang, X. Meng, Y. Yin, Y. Wang, X. Yang, X. Zhang, X. Peng, W. He, G. Dong, H. Chen, Optical image watermarking based on singular value decomposition ghost imaging and lifting wavelet transform. Opt. Lasers Eng. **114**, 76–82 (2019)
33. J. Zhang, J. Erway, X. Hu, Q. Zhang, R. Plemmons, Randomized SVD methods in hyperspectral imaging. J. Electr. Comput. Eng. **2012**, 3–3 (2012)
34. M. Hénon, A two-dimensional mapping with a strange attractor. Theory Chaot. Attract. 94–102 (2004)
35. S. Ibrahim, A. Alharbi, Efficient image encryption scheme using Henon map, dynamic S-boxes and elliptic curve cryptography. IEEE Access **8**, 194289–194302 (2020)
36. W. Zhao, Z. Zhang, L. Wang, Manta ray foraging optimization: an effective bio-inspired optimizer for engineering applications. Eng. Appl. Artif. Intell. **87**, 103300 (2020)
37. The National Library of Medicine presents MedPix. A free online Medical Image Database available at https://medpix.nlm.nih.gov/home.
38. M. Ali, C.W. Ahn, An optimal image watermarking approach through cuckoo search algorithm in wavelet domain. Int. J. Syst. Assur. Eng. Manag. **9**, 602–611 (2018)
39. S. Roy, A.K. Pal, An SVD based location specific robust color image watermarking scheme using RDWT and Arnold scrambling. Wirel. Pers. Commun. **98**, 2223–2250 (2018)
40. S. Thakur, A.K. Singh, B. Kumar, S.P. Ghrera, Improved DWT-SVD-based medical image watermarking through hamming code and chaotic encryption. Adv. VLSI, Commun., Signal Process.: Select Proceed. VCAS **2018**, 897–905 (2020)